On the relations between fracture energy and physical observables in dynamic earthquake models

Andrea Bizzarri[1]

Received 5 October 2009; revised 29 April 2010; accepted 2 June 2010; published 16 October 2010.

[1] We explore the relationships between the fracture energy density (E_G) and the key parameters characterizing earthquake sources, such as the rupture velocity (v_r), the total fault slip (u_{tot}), and the dynamic stress drop ($\Delta\tau_d$). We perform several numerical experiments of three-dimensional, spontaneous, fully dynamic ruptures developing on planar faults of finite width, obeying different governing laws and accounting for both homogeneous and heterogeneous friction. Our results indicate that E_G behaves differently, depending on the adopted governing law and mainly on the rupture mode (pulselike or cracklike, sub- or supershear regime). Subshear, homogeneous ruptures show a general agreement with the theoretical prediction of $E_G \propto \sqrt{1-\left(v_r^2/v_S^2\right)}$, but for ruptures that accelerate up to supershear speeds it is difficult to infer a clear dependence of fracture energy density on rupture speed, especially in heterogeneous configurations. We see that slip pulses noticeably agree with the theoretical prediction of $E_G \propto u_{\mathrm{tot}}^2$, contrarily to cracklike solutions, both sub- and supershear and both homogeneous and heterogeneous, which is in agreement with seismological inferences, showing a scaling exponent roughly equal to 1. We also found that the proportionality between E_G and $\Delta\tau_d^2$, expected from theoretical predictions, is somehow verified only in the case of subshear, homogeneous ruptures with RD law. Our spontaneous rupture models confirm that the total fracture energy (the integral of E_G over the whole fault surface) has a power law dependence on the seismic moment, with an exponent nearly equal to 1.13, in general agreement with kinematic inferences of previous studies. Overall, our results support the idea that E_G should not be regarded as an intrinsic material property.

Citation: Bizzarri, A. (2010), On the relations between fracture energy and physical observables in dynamic earthquake models, *J. Geophys. Res.*, *115*, B10307, doi:10.1029/2009JB007027.

1. Introduction

[2] The so-called "fracture" energy density, E_G (where $[E_G]$ = J/m^2), is recognized to be one of the most important parameters in the context of the physics of the earthquake source and directly influences earthquake dynamics, since its value controls the rupture propagation and its arrest [*Husseini et al.*, 1975; *Schmedes et al.*, 2010]. In addition, it affects radiation efficiency [e.g., *Husseini and Randall*, 1976; *Venkataraman and Kanamori*, 2004]. In recent years, many efforts have been made in order to retrieve its value from laboratory experiments [e.g., *Wong*, 1982; *Lockner and Okubo*, 1983] as well as from seismological inferences [*McGarr et al.*, 2004; *Tinti et al.*, 2005, and references therein] and to try to establish some analytical or empirical relations between E_G and macroscopic physical observables, such as the scalar seismic moment (M_0), the rupture velocity of the propagating crack front (v_r), and stress drop.

[3] E_G can be physically defined as the amount of energy (for unit fault surface) necessary to maintain an ongoing rupture which propagates on a fault (or alternatively, as the work done against the resistance to fault extension at the rupture tip). It is often called seismological fracture energy density and has been denoted with symbol G (or G_c) in a large number of previous papers. In the framework of linear elastic fracture mechanics (LEFM) it has been associated with critical stress intensity factors [*Irwin*, 1957; *Broberg*, 1999; *Tada et al.*, 2000] for different modes of crack propagation, which are material parameters and depend on the temperature and pressure conditions, grain size, etc. [e.g., *Paterson and Wong*, 2005]. The understanding of the earthquake energy budget (i.e., the quantification of the amounts of energy dissipated during cosesimic ruptures by the production of new fracture surfaces, by seismic wave emission, thermal processes, etc.) is one of the fundamental open issues in earthquake source physics [e.g., *Brown*, 1998].

[4] From a mathematical point of view, on a specific point on the fault, we can define E_G as the difference between the energy absorbed per unit area on the fault plane and the

[1]Istituto Nazionale di Geofisica e Vulcanologia, Sezione di Bologna, Bologna, Italy.

0148-0227/10/2009JB007027

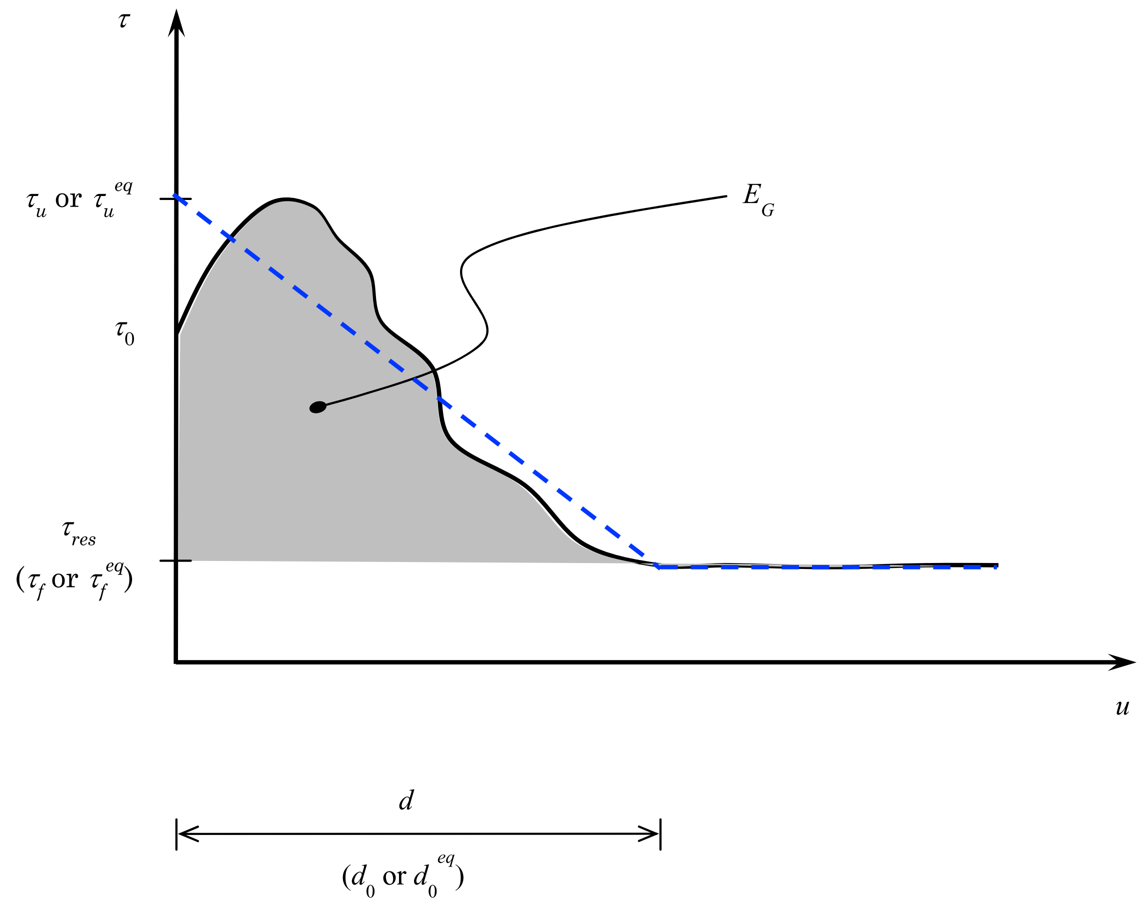

Figure 1. Sketch showing the geometrical interpretation of the fracture energy density E_G as defined in equation (1). In the traction versus slip curve, τ_0 is the magnitude of the initial shear stress and τ_{res} is its final level, attained when slip equals d. Dashed curve represents the traction behavior in the case of a linear slip-weakening constitutive equation.

work done against the frictional stress [e.g., *Bizzarri and Cocco*, 2006b] as

$$E_G \underset{\mathrm{df}}{=} \int_0^d (\tau - \tau_{res}) du, \tag{1}$$

where d is the amount of cumulative slip (u) at which the value of the magnitude τ (i.e., l^2-norm) of the fault shear traction $\mathbf{T}$ reaches the residual level of friction, τ_{res}, attained after the completion of the stress release. Figure 1 shows a typical traction behavior for increasing cumulative fault slip and the geometrical interpretation of the previous definition of E_G. Equation (1) implicitly assumes that τ has a dependence on u, which can be explicit, as for the slip-dependent friction laws [e.g., *Ida*, 1972] or implicit, as for other governing models. The quantity d in (1) can be associated with the characteristic distance d_0 in the context of the linear slip-weakening (SW) friction, or to its equivalent d_0^{eq} (see *Cocco and Bizzarri* [2002] for a detailed discussion) in the framework of the laboratory-derived rate- and state-dependent (RS) governing laws [e.g., *Ruina*, 1983] or, more generally, in the case of other nonlinear constitutive equations. Analogously, the quantity τ_{res} in (1) can be associated with the kinetic level of friction, τ_f, in the case of the SW law, or to its equivalent τ_f^{eq} [see *Bizzarri and Cocco*, 2003], in the case of RS laws. In general, we can regard τ_{res} as the value that the fault friction attains when the all the dissipative, chemicophysical processes occurring during the cosesimic breakdown phase are completed [*Bizzarri and Cocco*, 2006a, 2006b] (see *Bizzarri* [2009b] for a comprehensive review). As defined in (1), in general E_G is not a prior-imposed constitutive property but is determined by the dynamic time evolution of the total traction.

[5] If the considered fault is governed by the linear SW law (see the dashed curve in Figure 1), then equation (1) is simply reduced to [see *Palmer and Rice*, 1973]

$$E_G = \Delta\tau_b \frac{d_0}{2}, \tag{2}$$

which depends only on constitutive parameters ($\Delta\tau_b \underset{\mathrm{df}}{=} \tau_u - \tau_f$ is the breakdown stress drop, with τ_u being the upper yield stress); in this case E_G is a prior-imposed property. If $\Delta\tau_b$ and d_0 are homogeneous over the whole fault surface, then also E_G is spatially constant, even if there are no theoretical requirements for that. Moreover, when τ_f is a well-defined level, it is apparent from (2) that E_G can be interpreted as the energy in excess of the energy required to sustain frictional sliding at shear level τ_f.

[6] In the framework of the RS laws, equation (2) can be rewritten as

$$E_G \cong b\sigma_n^{\text{eff}}\left[\ln\left(\frac{v_2}{v_0}\right)\right]^2 \quad \frac{L}{2}, \tag{3}$$

where b is a constitutive parameter, σ_n^{eff} is the effective normal stress, L is the scale length for the evolution of the state variable, v_0 is the initial fault slip velocity, and v_2 is its value (a priori unknown) after the breakdown process. For analytical details, see *Bizzarri and Cocco* [2003].

[7] When isotropic friction is not assumed, that is, when the fault shear traction vector $\mathbf{T}$ is not collinear to fault slip velocity vector $\mathbf{v}$ (namely, when $\mathbf{T} \neq ||\mathbf{T}||v/||v||$), as is usually assumed in spontaneous dynamic earthquake models (*Bizzarri and Cocco* [2005], among others), equation (1) has been generalized as [*Tinti et al.*, 2005]

$$E_G = \int_0^{T_b} (\mathbf{T} - \mathbf{T}_{\text{res}}) \bullet \mathbf{v}\, dt, \tag{4}$$

where T_b is breakdown duration (i.e., the time interval over which the stress release is realized), $\mathbf{T}_{\text{res}}$ is the residual shear traction vector (its Euclidean norm is the quantity τ_{res} in (1)), t is the time and the bullet symbol indicates the scalar product. *Tinti et al.* [2005] term the quantity expressed by equation (4) breakdown work, even if, strictly speaking, it accounts also for the energy spent before the beginning the breakdown phase (i.e., during the possible early strengthening stage of the rupture, where the fault traction increases for increasing slip or slip velocity).

[8] The total fracture energy, U_G (where $[U_G]$ = J) is the integral of E_G defined by equation (1) or (4) over the whole fault surface as

$$U_G = \iint_{\Sigma} E_G(\boldsymbol{\xi}) d\boldsymbol{\xi}, \tag{5}$$

where $\boldsymbol{\xi}$ maps the fault surface Σ. It is apparent that while the quantity E_G is a local estimate, which can be spatially variable as a consequence of the heterogeneous distribution of shear traction and slip velocity, U_G is a global estimate, which characterizes the whole seismic rupture event.

[9] Although some authors have considered the surface energy (i.e., the amount of energy spent in creating new sliding surfaces; in other words, the energy needed to break bonds) as the same physical quantity as the fracture energy [*Wilson et al.*, 2005; *Yoshioka*, 1996], after the studies of *Chester et al.* [2005], *Tinti et al.* [2005], and *Pittarello et al.* [2008] it is now clear that surface energy is only a small fraction of the mechanical work absorbed on the fault [see also *Lockner and Okubo*, 1983]. *Pittarello et al.* [2008] also show that the most prominent fraction of E_G,which in turn is not a negligible contribution to the earthquake energy budget [*Venkataraman and Kanamori*, 2004; *Tinti et al.*, 2005; *Cocco et al.*, 2006], is represented by heat produced by frictional sliding. Moreover, we emphasize that E_G is not only due to interfacial friction, but it is the sum of all energies associated with breakdown mechanisms.

2. Existing Scaling Relations for Fracture Energy

[10] From laboratory experiments of initially intact rock fracture and mode II shear failure on preexisting faults (precut samples) loaded by a two-axial apparatus, *Ohnaka* [2003] through his equation (22) proposes a linear dependence of E_G on the characteristic wave length λ_c of the topography of the sliding surface at which its self-similarity breaks down as

$$E_G = 0.281\ \tau_{\text{u}} \left(\frac{\Delta\tau_b}{\tau_{\text{u}}}\right)^{1.83} \lambda_{\text{c}}. \tag{6}$$

In the context of a constitutive model different from the SW law, the quantities τ_u and τ_f have to be regarded as their equivalents, τ_u^{eq} and τ_f^{eq}, respectively [see *Bizzarri and Cocco*, 2003].

[11] The obvious scale dependence of the parameter λ_c makes E_G also scale dependent. This scale dependence [see *Ionescu and Campillo*, 1999] is furthermore apparent from equation (1), where it is stated as an explicit dependence of the fracture energy density on the length scale d. On the other hand, *Otsuki* [2007] found that the average fracture energy density is proportional to the length of a seismic rupture zone to the power of 0.56.

[12] By considering a slip pulse [*Freund*, 1979] obeying the position-weakening friction law introduced by *Palmer and Rice* [1973] (in this simplified form of the SW law, the traction linearly degrades with increasing spatial position of the rupture tip), *Rice et al.* [2005] through their equation (17), found, in two-dimensions (2D), a relationship between E_G, the total cumulative slip u_{tot} developed during the time duration of the pulse (t_{pulse}), and the rupture velocity as

$$E_G = \frac{G u_{\text{tot}}^2}{\pi L_{\text{pulse}}} F(v_r), \tag{7}$$

where L_{pulse} is the spatial length of the pulse, which can be approximated as $L_{\text{pulse}} \cong \langle v_r \rangle\ t_{\text{pulse}}$ (where $\langle v_r \rangle$ is the average rupture velocity), G is the rigidity of the medium, and the dimensionless function $F(v_r)$ depends on the rupture modes and is defined as

$$F(v_r) = \begin{cases} \dfrac{R}{\alpha_S\left(1-\alpha_S^2\right)} & \text{, for mode II} \\ \alpha_S & \text{, for mode III} \end{cases} \tag{8}$$

[see also *Rice et al.*, 2005, equation (11)]. In equation (8) $R \equiv 4\alpha_S\alpha_P - (1 + \alpha_S^2)^2$ is 4 times the Rayleigh function, $\alpha_S \equiv \sqrt{1-\left(v_r^2/v_S^2\right)}$ and $\alpha_P \equiv \sqrt{1-\left(v_r^2/v_P^2\right)}$ (v_S and v_P being the S and P wave speeds, respectively). A similar dependence of E_G on v_r was also reported by *Day* [1982] in his equation (11). Moreover, $F(v_r)$ monotonically decreases for increasing v_r with maximum value for $v_r = 0$, where it equals $1/(1 - \nu)$ or 1 in the case of mode II or mode III, respectively (ν is the Poisson ratio).

[13] The dependence of E_G on u_{tot} contained in equation (7) roughly agrees with the empirical estimates of

Zhang et al. [2003], on the basis of the SW curves inferred from data of the 1999 Chi-Chi earthquake, as

$$E_G = 0.35 \times 10^6 u_{\mathrm{tot}}^{2.2}. \tag{9}$$

[14] On the other hand, *Abercrombie and Rice* [2005] by fitting earthquake data for slip ranging from 0.2 mm to 0.2 m to their equation (5) found the slightly different relation

$$E_G = 5.25 \times 10^6 \; u_{\mathrm{tot}}^{1.28}. \tag{10}$$

McGarr et al. [2004] in their equation (7), using a crack model, suggest that fracture energy is linearly related to slip, while laboratory experiments by *Chambon et al.* [2006, equation (10)] suggest a still lower scaling exponent (~0.6).

[15] From the nonspontaneous (i.e., with an a priori-assigned and constant v_r), 2D plane-strain, self-similar solution of *Burridge* [1973], *Andrews* [1976b] (p. 5685) obtains an expression for fracture energy density as

$$E_G = \frac{\pi r}{4\mathrm{G}} K(v_r) \; Q(v_r) \; \Delta\tau_d^2, \tag{11}$$

where r is the distance of the rupture tip from the nucleation point (i.e., the length of the crack from the nucleation point), $K(v_r)$ and $Q(v_r)$ are dimensionless functions of the rupture velocity, and $\Delta\tau_d \underset{\mathrm{df}}{=} \tau_0 - \tau_f$ is the dynamic stress drop (τ_0 denotes the initial shear stress). The square dependence of E_G on $\Delta\tau_d$, postulated also by *Kostrov* [1964], recalls the proportionality of E_G to $\Delta\tau_b^{1.83}$ contained in equation (6). The dependence of E_G on v_r in (11) can be made more explicit by considering equations (7) and (23) of *Ida* [1972], that give [see *Andrews*, 1976a, equation (23)]

$$E_G = \frac{\pi r}{2G} \; B(v_r) \; \alpha_S \; \Delta\tau_d^2, \tag{12}$$

where α_S has been defined above and $B(v_r)$ is a dimensionless, monotonic function of v_r. Since $B(v_r)$ can be approximated as $2/\pi$ [see *Andrews*, 1976a], equation (12) can be rewritten as

$$E_G \cong \frac{r}{G} \; \alpha_S \; \Delta\tau_d^2. \tag{13}$$

This relation is equivalent to equation (11.24) of *Aki and Richards* [2002], derived in the case of a semi-infinite mode III shear model with cohesive force. A similar expression for E_G,

$$E_G = \frac{r}{\pi G} \; \frac{1}{\alpha} \; \Delta\tau_d^2, \tag{14}$$

from equation (7) of *Wong* [1982], has been also used by *Husseini et al.* [1975] with $\alpha = 1$ in the case of a semi-infinite longitudinal shear crack.

[16] An important distinction between equation (7) and equations (12–14) is that the former is appropriate for a pulselike solution (in which the fault slip heals and the slip velocity has a finite duration), while the latter refer to a cracklike solution (where the slip does not spontaneously heal and the rupture continues to develop until the ends of the fault are reached or frictional heterogeneities are encountered).

[17] We finally mention that the kinematic models of *Tinti et al.* [2005] suggest that U_G scales with M_0 as

$$U_G \propto M_0^p, \tag{15}$$

where the exponent p is 1.18. This power law dependence, which links two quantities representative of the entire faulting episode, is in agreement with the fit of *Abercrombie and Rice* [2005] based upon observations arising from several real-world earthquakes; rewriting our equation (5) as $U_G = A\langle E_G\rangle$ (where $\langle E_G\rangle$ is the average fracture energy density over the cracked area A) and expressing $\langle E_G\rangle$ as in equation (5) of *Abercrombie and Rice* [2005], after simple algebra we have

$$U_G \;\cong\; \frac{5.25 \times 10^6}{G^q A^{q-1}} \; M_0^q \tag{16}$$

with a scaling exponent $q = 1.28$. (Note that we neglect both overshoot and undershoot phenomena, so that the quantity G' of *Abercrombie and Rice* [2005] is in fact our E_G. Moreover, we express the average fault slip S in equation (5) of *Abercrombie and Rice* [2005] as a function of the scalar seismic moment ($S = M_0/(G\,A)$ [e.g., *Aki*, 1967]). On the other hand, from equation (1) of *Venkataraman and Kanamori* [2004] we have

$$U_G \;\cong\; \frac{C}{2G\,A^{3/2}} \; M_0^2 \;-\; U_R \tag{17}$$

where C is a dimensionless constant ($C \cong 1.4$) and U_R is the (total) radiated energy (which is defined as the wave energy that would be transmitted to infinity if an earthquake occurred in an infinite, lossless medium) [*Haskell*, 1964]. Equations (15) to (17) suggest that fracture energy measured at the laboratory scale is several orders of magnitude smaller that that inferred for earthquakes [see also *Chester et al.*, 2005].

3. Limitations of the Theoretical Predictions and Motivation of the Present Paper

[18] Equations (7), (11), (12), and (13) previously discussed have been derived within the framework of the LEFM and by the identification of the limiting rupture speed of a propagating crack tip singularity. One important limitation of the above-mentioned equations we want to emphasize is that they have been (necessarily) obtained under the general assumption of simple 2D ruptures (or pulses). For example, equations (7) and (8) provide a relationship between E_G and v_r in the case of mode II ruptures only for $v_r \le v_R$ (from (7) and (8) we have that E_G becomes negative for $v_r > v_R$, where v_R indicates the Rayleigh speed) and in the case of mode III ruptures only for $v_r \le v_S$ (from the definition of α_S we have from equations (7), (12), and (13) that E_G assumes complex values for $v_r > v_S$). Indeed, *Bhat et al.* [2007] observe that for supershear slip pulses it is not possible to express E_G as a simple analytical expression of v_r (as in the subshear case); they numerically found (their Figure 14) that E_G initially increases for $v_S < v_r \lessapprox 1.3 v_S$ and then decreases for $1.3 v_S \lessapprox v_r \le v_P$. For steady state 2D shear cracks the velocity range between v_R and v_S is energetically inadmissible and therefore we cannot retrieve

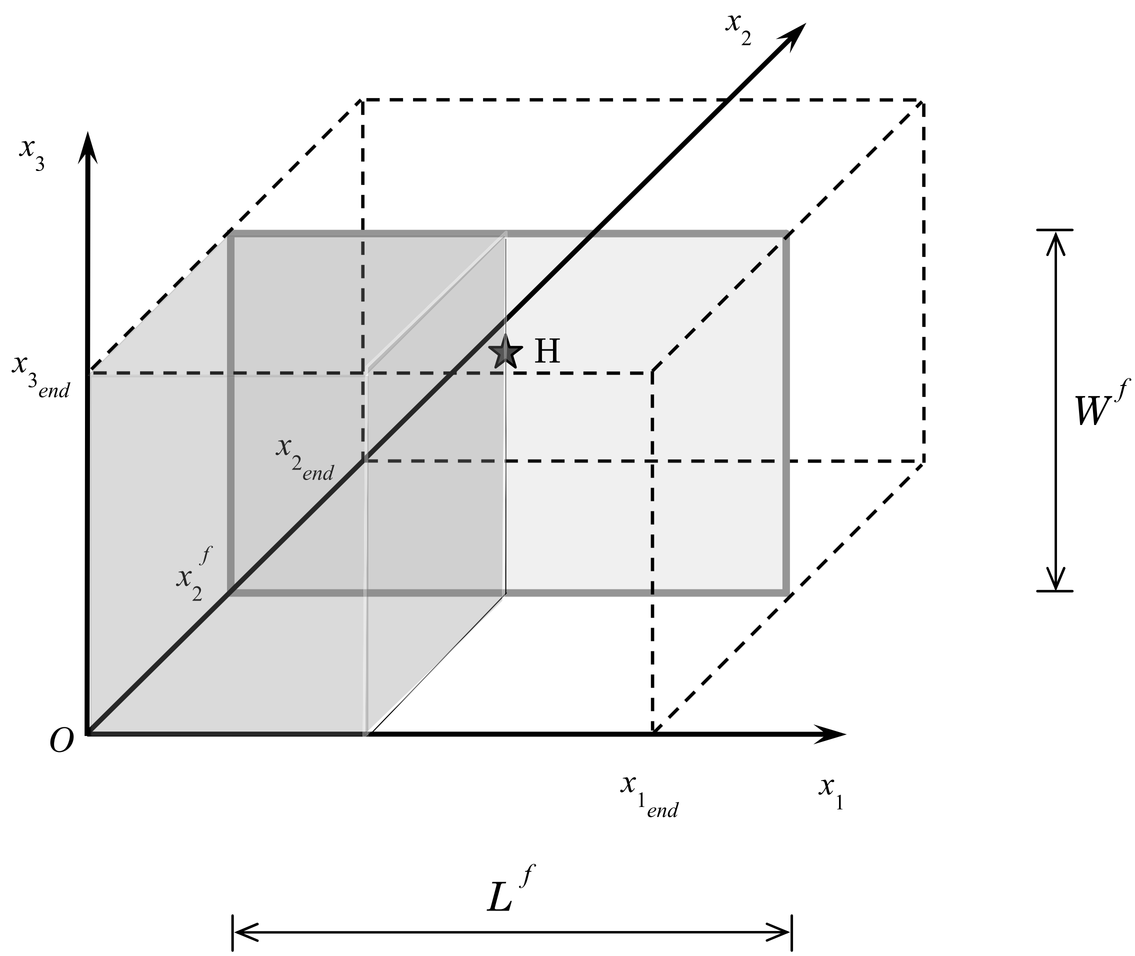

Figure 2. Geometry of the model. The imposed hypocenter is indicated by H and the light shaded plane indicates the fault $x_2 = x_2^f$, having aspect ratio L^f/W^f. The shaded box marks the portion of the computational domain where calculations are performed, due to the exploitation of the symmetry about H and about the fault plane.

any information in this velocity interval from the theoretical equations previously described.

[19] On the other hand, kinematic models contain only constraints on the average rupture velocity on a mathematical fault plane, ideally neglecting all possible small scale heterogeneities in geometrical path, such as branching, bending, and kinks, which have been introduced in dynamic models (e.g., E. M. Dunham et al., Earthquake ruptures with strongly rate–weakening friction and off–fault plasticity: 2. Nonplanar faults, submitted to *Bulletin of the Seismological Society of America*, 2010). More importantly, they cannot account for possible fluctuations of rupture velocity at periods shorter than those used to invert seismograms (limited frequency bandwidth limitation) and they finally suffer intrinsic limitations in representing the physics of earthquake rupture. Moreover, in all models of *Tinti et al.* [2005] v_r is almost uniform and they do not give an estimate of the dependence of E_G on v_r.

[20] As a natural consequence of the aforementioned limitations, in the present paper we mainly aim to explore whether fully dynamic, spontaneous models of earthquake ruptures developing on planar fault of finite extension indicate some specific relationships between fracture energy density and physical observables. In addition, we examine whether theoretical predictions based on some specific assumptions can be used also in more complex configurations. We will also investigate whether the behavior of fracture energy density is affected by the choice of the fault governing law and by the assumed spatial distribution of the initial shear stress on the fault surface.

[21] We finally remark that the calculations presented in this paper do not include inelastic deformations occurring near the rupture front. We also neglect the energy loss due to off-fault damage which increases the fracture energy density, but it can be adequately modeled by fracture energy on the fault [*Andrews*, 2005]. We do not consider zones of plastic deformation developing before the crack grows, nor viscous flow due to melting, so that there is no need to consider Elastic Plastic Fracture Mechanics (EPFM).

4. Rupture Simulations

[22] In this paper, we solve the fundamental elastodynamic equation, neglecting body forces, for a single, planar, strike-slip fault embedded in a perfectly elastic, isotropic half-space with free surface condition. The adopted fault

Table 1. Model Discretization and Constitutive Parameters Adopted in This Study

Parameter	Value
Medium and Discretization Parameters	
Lamé constants, $\lambda = G$	27 GPa
S wave velocity, v_S	3 km/s
P wave velocity, v_P	5.196 km/s
Cubic mass density, ρ	3000 kg/m^3
Fault length, L^f	12 km
Fault width, W^f	11.6 km
Spatial grid size, $\Delta x_1 = \Delta x_2 = \Delta x_3 \equiv \Delta x$	8 m[a]
Time step, Δt	4.44×10^{-4} s
Courant-Friedrichs-Lewy (CFL) ratio $\omega_{\mathrm{CFL}} \underset{\mathrm{df}}{=} v_S \Delta t / \Delta x$	0.1665
Coordinates of the hypocenter $H \equiv (x_1^H, x_3^H)$	(5.992,7) km
Domain boundary conditions	$x_1 = 0$: ABC[b]; $= x_1^H$: symmetry[c] $x_2 = 0$: ABC[b]; $= x_2^f$: symmetry[c] $x_3 = 0$: Free surface; $= x_{3\mathrm{end}}$: ABC[b]
Fault Constitutive Parameters	
Initial rake angle, φ_0	0°[d]
Effective normal stress, σ_n^{eff}	120 MPa
Slip-Weakening Law (Equation (18))	
Magnitude of the initial shear stress, τ_0	70.51572 MPa[e]
Static level of friction coefficient, μ_u	0.73167 ($\leftrightarrow \tau_u = 87.80$ MPa)[f]
Kinetic level of friction coefficient, μ_f	0.54333 ($\leftrightarrow \tau_f = 65.20$ MPa)[f]
Dynamic stress drop, $\Delta\tau_d \underset{\mathrm{df}}{=} \tau_0 - \tau_f$	5.32 MPa
Breakdown stress drop, $\Delta\tau_b \underset{\mathrm{df}}{=} \tau_u - \tau_f$	22.60 MPa
Strength parameter $S \underset{\mathrm{df}}{=} (\tau_u - \tau_0)/(\tau_0 - \tau_f)$	3.25
Characteristic slip-weakening distance, d_0	0.05 m[f]
Ruina-Dieterich Law (Equation (19))	
Logarithmic direct effect parameter, a	0.016
Evolution effect parameter, b	0.020
Scale length for state variable evolution, L	0.02 m
Reference value of friction coefficient at low slip rates, μ_*	0.56
Initial sliding velocity, v_0	1×10^{-4} m/s
Magnitude of the initial shear stress, τ_0	$\mu^{ss}(v_0)\ \sigma_n^{eff} = 70.51572$[g]
Ruina-Dieterich Law With Flash Heating of Asperity Contacts (Equation (20))	
Reference value of friction coefficient at high slip rates, μ_{fh}	0.13
Initial sliding velocity, v_0	1×10^{-4} m/s
Magnitude of the initial shear stress, τ_0	$\mu^{ss}(v_0)\ \sigma_n^{eff} = 70.51572$[g]

[a]Fine spatiotemporal discretization guarantees a proper resolution of the breakdown zone (see *Bizzarri*, [2009a] for numerical details) for all of the considered governing models. This allows the analysis of ruptures up to a frequency $f_{\mathrm{acc}}^{(s)} = v_S/(6\Delta x) = 62.5$ Hz and what is more, it guarantees not less than 40 points within the breakdown zone (on average, for all considered numerical simulations), that in turn ensures a stable determination of fracture energy density in each fault node.

[b]Absorbing boundary conditions described by *Bizzarri and Spudich* [2008, Appendix A].

[c]Symmetries about the strike location of the hypocenter ($x_1 = x_1^H$) and about the fault ($x_2 = x_2^f$) are exploited as described by *Bizzarri* [2009a].

[d]For sake of simplicity the initial shear traction vector is aligned along x_1.

[e]This value has been chosen to have the same initial shear stress for all governing models in case of homogeneous conditions.

[f]These values correspond to the average values of τ_u^{eq}, τ_f^{eq} and d_0^{eq} of the homogeneous RD simulation.

[g]The μ^{ss} denotes the steady state value of the friction coefficient, realized when $\mathrm{d}\Theta/\mathrm{d}t = 0$ in the evolution equations of models (19) and (20).

Figure 3. Solution for a synthetic subshear earthquake, obeying the RD law (equation (19)), and for a homogeneous distribution of the initial shear stress. Distribution on the fault plane at the final time level of the numerical simulation of (a) cumulative fault slip u_{tot}, (b) fault slip velocity v, (c) fault traction τ, (d) rupture velocity v_r, and (e) E_G. The insets in Figures 3a–3c report the behavior of u_{tot}, v, and τ, respectively, as functions of the strike coordinate, at the hypocentral depth. Rupture velocities are calculated as in equation (12) of *Bizzarri and Spudich* [2008] using $v_r(x_1,x_3) = 1/\| \nabla_{(x_1,x_3)} t_r(x_1,x_3)\|$, where t_r is the rupture time, defined as the instant of time at which the fault slip velocity exceeds a threshold value v_l, assumed to be 0.01 m/s. In Figures 3a, 3b, 3d, and 3e purple color denotes unbroken part of the fault plane. Note that due to symmetry exploitation only one-half of the fault along the strike direction is reported on the plots (the same holds for Figures 10a, 10c, 10d, 11).

geometry is shown in Figure 2. The problem is solved numerically, by employing the three-dimension (3D), second order accurate, OpenMP-parallelized, finite difference, conventional grid code described by *Bizzarri and Cocco* [2005]. The absorbing boundary conditions described in *Bizzarri and Spudich* [2008] are adopted in order to reduce spurious reflections from the borders of the computational domain and the existing symmetries are exploited to reduce

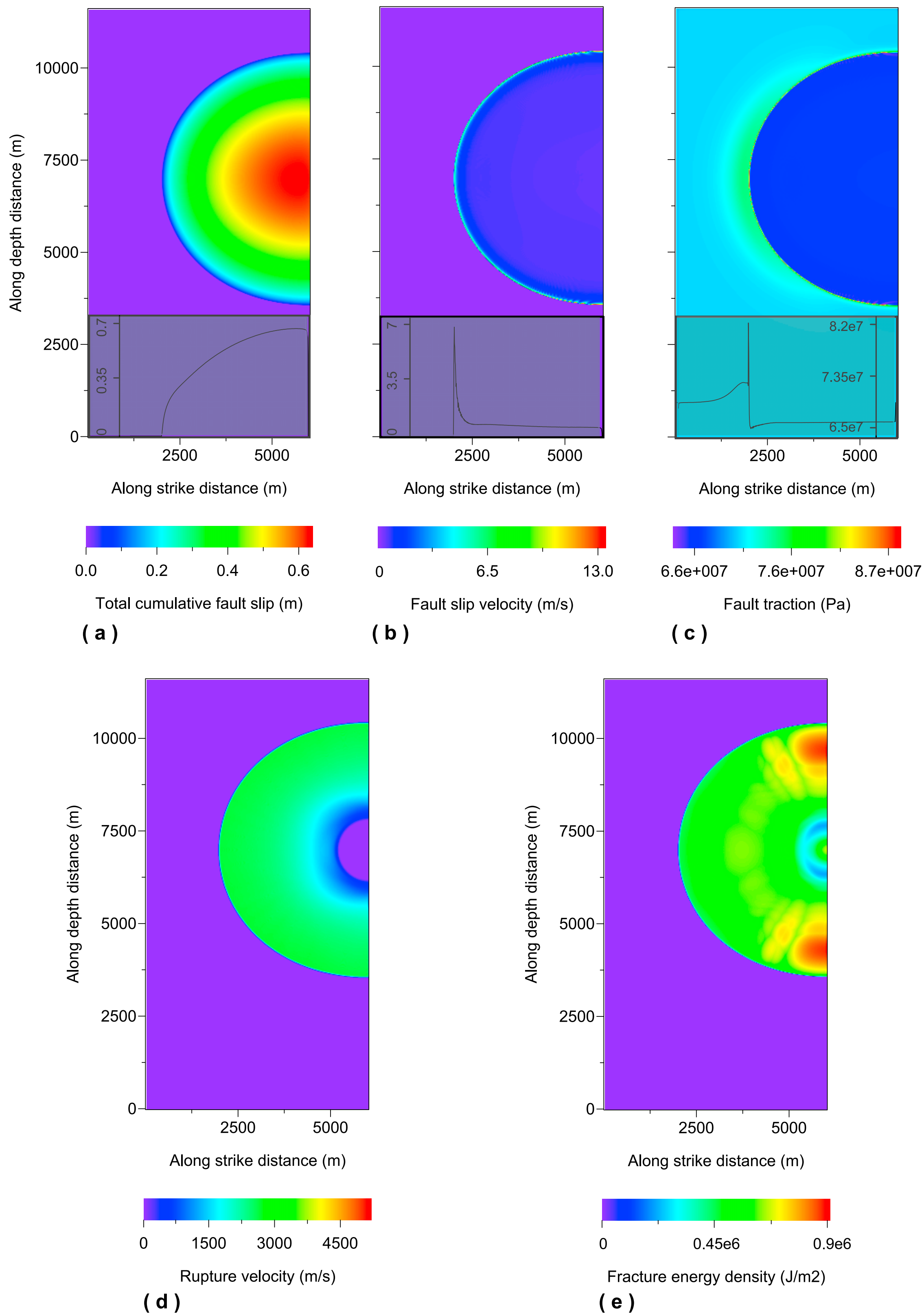

Figure 3

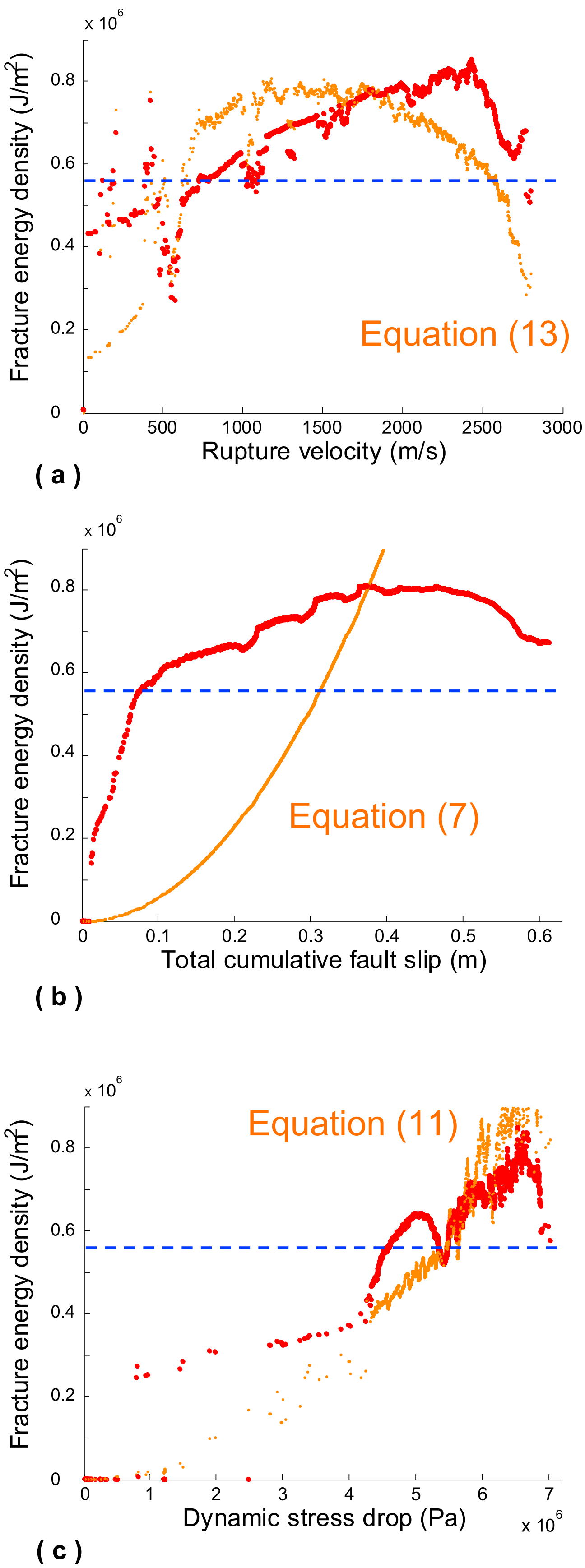

computational times and storage requirements, as discussed in detail by *Bizzarri* [2009a]. The rupture starts from the hypocenter H and expands bilaterally in a spontaneous fashion and dynamically; the slip is purely tangential, so that no opening or interpenetration of material is allowed. Within an initialization patch I_{nucl} surrounding H, the earthquake nucleation is realized by initially forcing the rupture to develop with a constant speed in the case of the SW law. For the RS law, on the contrary, the nucleation is obtained by decreasing at $t = 0$ the value of the state variable, by setting a value smaller than the steady state attained outside I_{nucl}. Additional numerical details are presented by *Bizzarri* [2010a] and *Bizzarri* [2009a].

[23] The fault boundary condition on the frictional interface is represented by the constitutive law (in this study we consider a wide range of governing models): under the linear SW law,

$$\tau = \begin{cases} \tau_u - (\tau_u - \tau_f)\dfrac{u}{d_0} & , u < d_0 \\ \tau_f & , u \geq d_0 \end{cases}, \tag{18}$$

[*Ida*, 1972], under the Ruina-Dieterich (RD) form of the RS law,

$$\begin{array}{l} \tau = \left[\mu_* + a\ln\left(\dfrac{v}{v_*}\right) + \Theta\right]\sigma_n^{\mathrm{eff}} \\ \dfrac{\mathrm{d}}{\mathrm{d}t}\Theta = -\dfrac{v}{L}\left[b\ln\left(\dfrac{v}{v_*}\right) + \Theta\right] \end{array}, \tag{19}$$

[*Bizzarri*, 2009a, and references therein] (Θ is the dimensionless state variable, a is a constitutive parameter, while μ_* and v_* are reference values for friction coefficient and sliding velocity, respectively), and under the RD law with the incorporation of the phenomenon of the flash heating (FH) of microscopic asperity contacts,

$$\begin{array}{l} \tau = \left[\mu_* + a\ln\left(\dfrac{v}{v_*}\right) + \Theta\right]\sigma_n^{\mathrm{eff}} \\ \dfrac{\mathrm{d}}{\mathrm{d}t}\Theta = -\dfrac{v}{L}\left[\Theta + b\dfrac{v_{fh}}{v}\ln\left(\dfrac{v}{v_*}\right) + \left(1 - \dfrac{v_{fh}}{v}\right)\left(a\ln\left(\dfrac{v}{v_*}\right) + \mu_* - \mu_{fh}\right)\right] \end{array} \tag{20}$$

[*Bizzarri*, 2009a, and references therein], where v_{fh} is the cutoff velocity above which FH operates (for $v \leq v_{fh}$ the evolution equation for Θ is that of the classical RD model (19)) and μ_{fh} is the reference value for friction coefficient at high slip velocities.

[24] The reference parameters adopted in this study (see Table 1) refer to a typical, subshear crustal earthquake. In the next two sections we will assume on the fault a homo-

Figure 4. Relations between fracture energy density and physical observables for the simulation reported in Figure 3. With red circles we report (a) E_G as a function of v_r, (b) E_G as a function of u_{tot}, and (c) E_G as a function of $\Delta\tau_d$. In orange are reported the values of E_G as obtained from theoretical predictions (equations (13), (7), and (11) for Figures 4a, 4b, and 4c, respectively). The dashed blue curve indicates the value of E_G for corresponding homogeneous SW model (equation (18)), as obtained from equation (2).

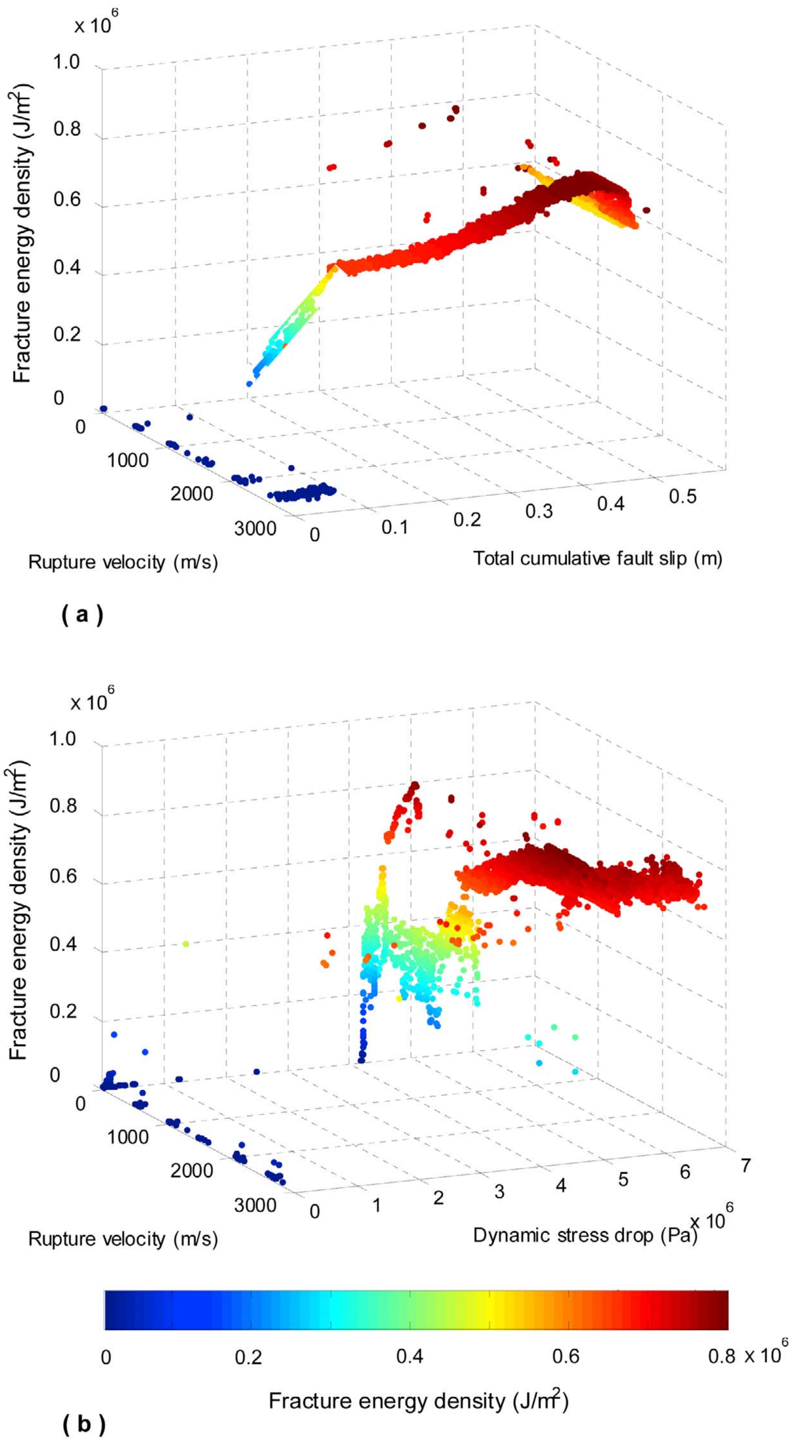

Figure 5. Three-dimensional scatter plots displaying the behavior of E_G as a function of the two independent variables appearing in equations (7) and (13), for the model reported in Figures 3 and 4. (a) $E_G = E_G(v_r, u_{\mathrm{tot}})$. (b) $E_G = E_G(v_r, \Delta\tau_d)$.

geneous initial shear stress, while in section 7 we will consider heterogeneous distributions.

5. Results for Homogeneous Configurations: Subshear Synthetic Earthquakes

[25] In homogeneous conditions, the linear SW model, equation (18), prescribes a constant fracture energy density over the whole fault; E_G is simply expressed by equation (2). On the contrary, within the framework of RS friction laws E_G can be spatially variable, due to the variability of shear traction on the fault, even for homogeneous τ_0.

[26] We report in Figure 3 the spatial distribution on the fault plane of the relevant quantities of our problem at the end of a numerical experiment. They pertain to a synthetic

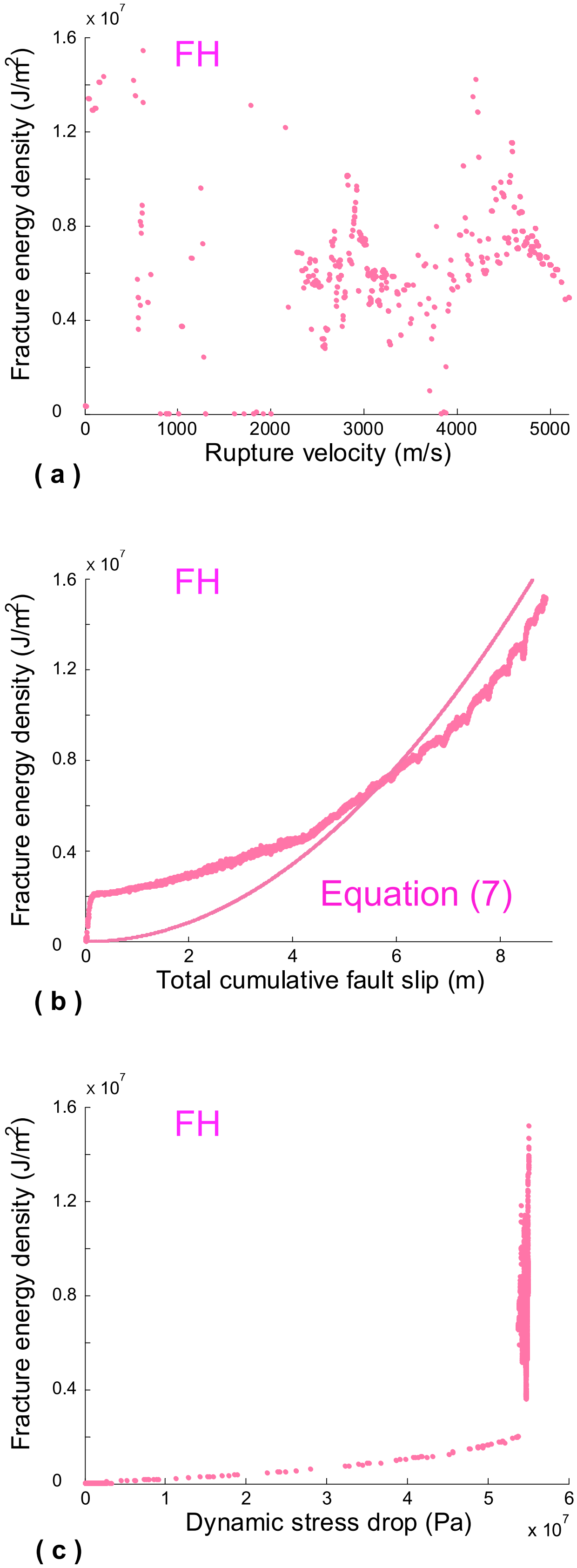

Figure 6. The same as in Figure 4, but now in the case of a supershear rupture obeying the FH governing law (equation (20)).

earthquake of moderate size (M_0 = 4.25 × 10^{17} Nm, corresponding to $M_w = (\mathrm{Log}(M_0) - 9)/1.5 = 5.8$) obeying the RD law, equation (19). In Figure 4 we plot, with red circles, the behavior of E_G, represented separately as a function of v_r, u_{tot} and $\Delta\tau_d$, resulting for this synthetic event. On the basis of our fine spatial discretization (see Table 1), in each synthetic event about one million points were considered for the analysis. We have performed a zero-offset spatial correlation analysis, in that we have considered the values of different quantities attained in the same fault node. We will discuss in the appendix the effects of a nonzero-offset correlation analysis, where the quantities are compared in different points of the rupture plane (i.e., we introduce some spatial offset).

[27] From Figure 4a we can see that the dependence of E_G on v_r is roughly described by equation (13) (orange dots); the fluctuations for low v_r (v_r < 500 m/s) refer to the nucleation phase, within the initialization patch I_{nucl}. Note that equation (13) in Figure 4a is plotted for the different values of $\Delta\tau_d$ realized in the different fault nodes. On the contrary, from Figure 4b we have that the proportionality of E_G to u_{tot}^2 theoretically predicted for pulses by equation (7) (orange dots) is markedly far from describing the numerical results (Figure 4b, red dots); this result is not surprising and we will discuss in the next section the reason for such a strong disagreement with the theoretical prediction. Finally, Figure 4c shows that the dependence of E_G on $\Delta\tau_d$ is somehow proportional to $\Delta\tau_d^2$, as expected from equation (11).

[28] In Figure 5 we report the 3D scatter plots of the fracture energy density as a function of the two independent variables appearing in equations (7) and (11). This kind of figure is complementary with respect to Figure 4; for example, by considering the data points in Figure 5a, we have that the projection on the $E_G - v_r$ plane gives Figure 4a, while the projection on the $E_G - u_{\mathrm{tot}}$ plane gives Figure 4b. (The same holds for Figure 5b.)

6. Homogeneous, Supershear Synthetic Earthquakes

[29] In this section we will consider three cases, representative of supershear seismic events, where the maximum speed asymptotically reaches the P wave velocity. Even though most natural earthquakes have subshear rupture velocities, there is increasing interest in supershear earthquakes, because they have some important and distinct features [*Bizzarri and Spudich*, 2008; *Dunham and Bhat*, 2008; *Bizzarri et al.*, 2010].

[30] One numerical simulation refers to the FH governing model (equation (20)), in which, if the local temperature of a microscopic asperity contact reaches a temperature at which thermally activated defects become highly mobile, then the contact will weaken. The inclusion of FH causes the transition to the supershear regime [*Bizzarri*, 2009a] for a rheology (that of Table 1) which would produce a subshear propagation in the absence of FH (see previous section). The results are reported in Figures 6 and 7. In the other two cases, the RD law (equation (19)) is adopted, but we change the value of governing parameters a, in order to increase the degree of instability of the fault and its propensity to accelerate up to supershear speeds [see also *Bizzarri et al.*, 2001].

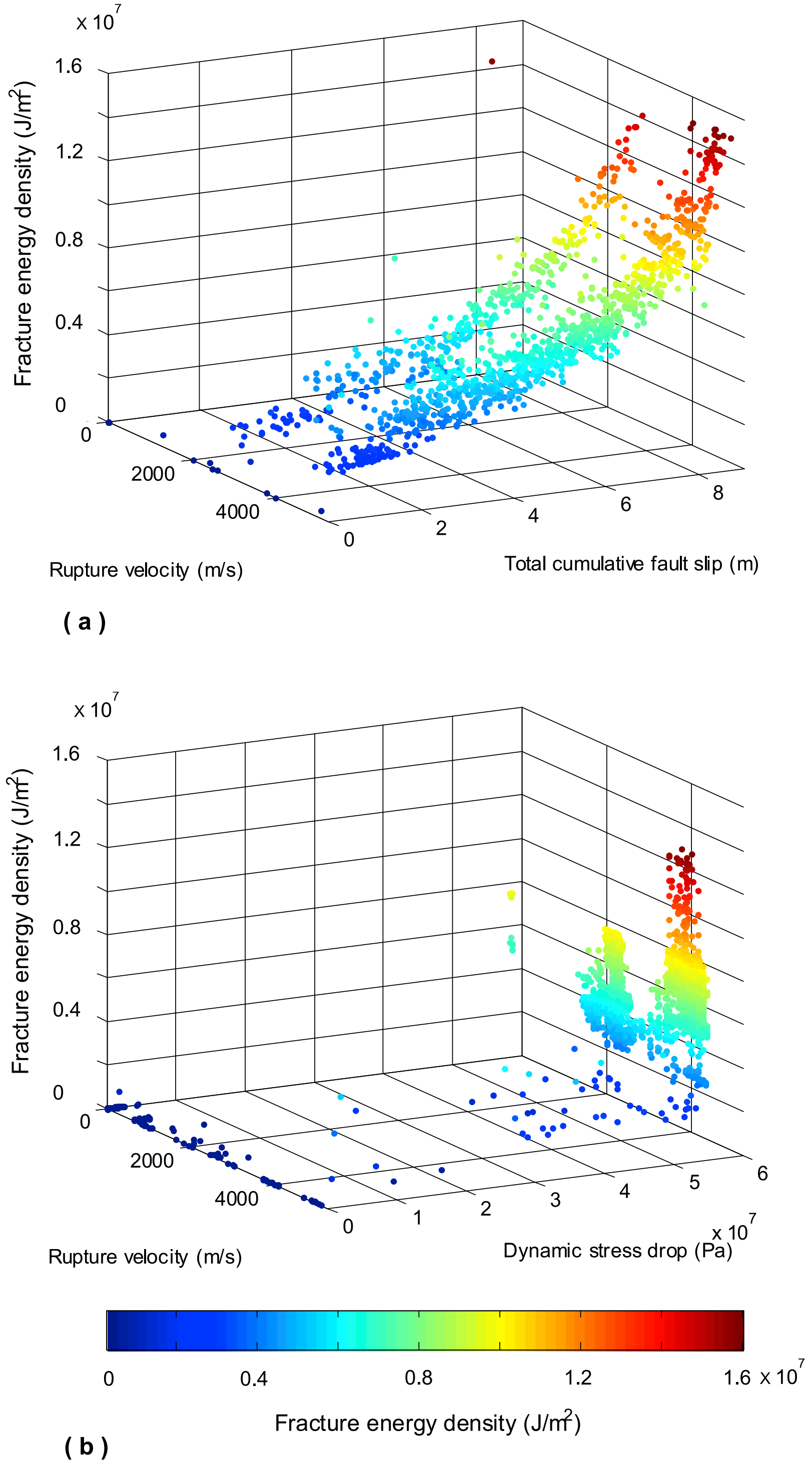

Figure 7. The same as in Figure 5, but now in the case of the FH model reported in Figure 6.

The results are displayed in Figures 8 and 9. Figure 8 compares the results obtained using a = 0.012 (full circles) and a = 0.010 and b = 0.022 (open circles). While the value of the initial shear stress in the FH case is the same as that adopted in the simulations discussed in the previous section, the different values of parameters a and b change the magnitude of τ_0 in the two RD numerical experiments.

[31] It is apparent from Figures 6a and 8a that the relationship between E_G and v_r becomes complicated in the case of supershear ruptures. In the FH case (Figure 6a) there is no a clear trend of E_G for increasing v_r, since the data are very sparse; they tend to group around two values of v_r, approximately at 2.5 km/s and 4.2 km/s (visible also in Figures 7a and 7b). In the RD cases (Figure 8a) it is possible

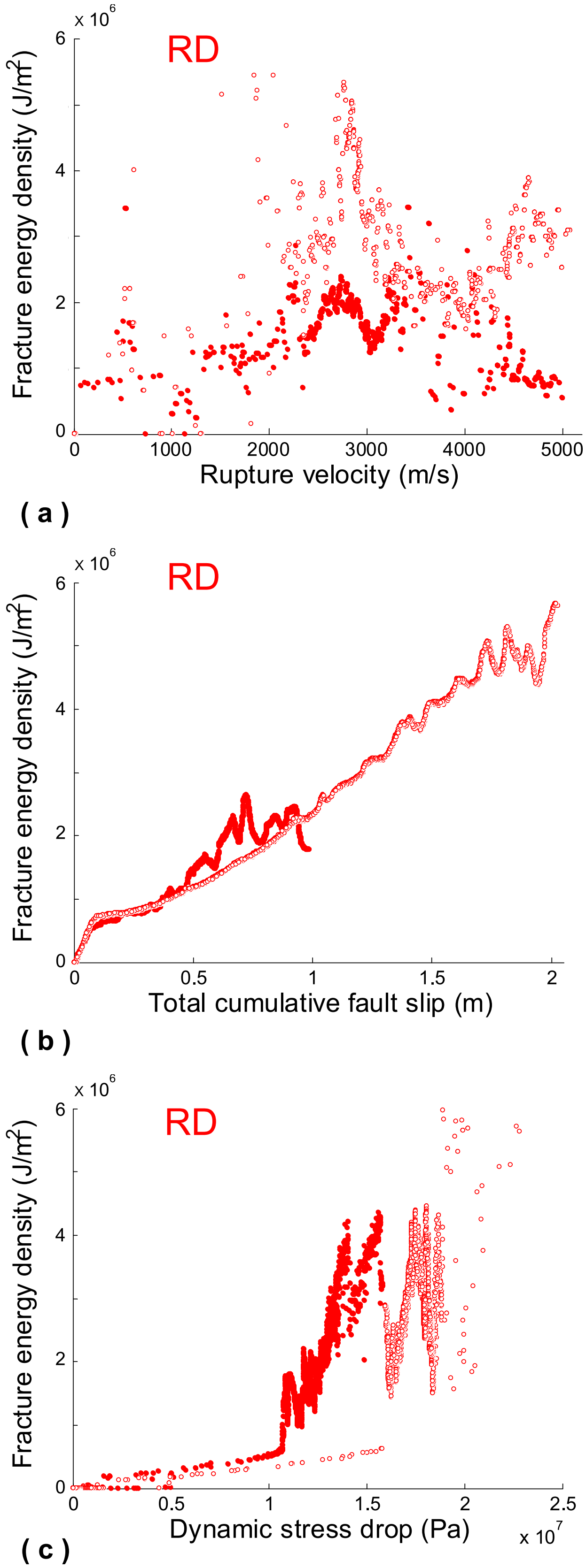

Figure 8. The same as in Figure 4, but now for two classical RD models (equation (19)). Full circles refer to a case with a = 0.012 and b = 0.020, while open circles refer to a case with a = 0.010 and b = 0.022.

to roughly envisage the behavior found by *Bhat et al.* [2007] in the case of supershear slip pulses. In our two spontaneous, dynamic ruptures with RD law there are large fluctuations of data and it is not simple to identify the value of rupture velocity which maximizes the fracture energy density; a rough estimate is that it is slightly smaller than v_S.

[32] An essential difference emerges from the comparison of the E_G versus u_{tot} curves (Figures 6b and 7a versus Figures 8b and 9a). We can see that the general agreement with equation (7) is quite good in the case of FH simulation (Figures 6b and 7a), but from the RD simulation shown in Figures 8b and 9a we have that E_G increases roughly in a linear fashion for increasing slip. We emphasize that in the FH case, for the adopted parameters, we have a pulselike solution, while in the two RD cases we have cracklike solutions (in these cases u_{tot} has to be interpreted as the slip at the end of the numerical experiments). Therefore, our fully dynamic simulations confirm that the prediction by *Rice et al.* [2005] is not appropriate in the case of sustained cracklike ruptures (see also Figures 4b and 5a). This result, which is also corroborated by the kinematic findings of *Tinti et al.* [2005], holds for other FH models where governing parameters produce slip pulses.

[33] In Figures 6c and 8c we plot the E_G versus $\Delta\tau_d$ curves. In the case of a sustained supershear slip pulse (Figures 6c and 7b) the value of τ_f^{eq} is substantially spatially constant. Considering that τ_0 is homogeneous, this causes the dynamic stress drop to be basically constant over the whole fault ($\Delta\tau_d \cong$ 55 MPa). This is apparent from Figures 6c and 7b, where we can see that the smaller values of $\Delta\tau_d$ correspond to very low values of the fracture energy density, attained basically within I_{nucl}. The fluctuations of E_G for $\Delta\tau_d \cong$ 55 MPa are due to the variations in traction evolution for slip below d_0^{eq} (recall equation (1)). In Figures 8c and 9b we can see that in these supershear ruptures E_G roughly increases linearly for increasing dynamic stress drop. In general, we can conclude that in both supershear cases, FH pulse and RD ruptures, the behavior predicted by equation (11) is not satisfied.

7. Do Heterogeneities Play a Role?

[34] Frictional sliding is usually a very irregular process, due to inhomogeneous conditions on the sliding surfaces [*Broberg*, 1978]. To account for this, following *Bizzarri et al.* [2010], in the present section we assume that the magnitude of the initial shear stress has a k^{-1} behavior at high wave numbers. Namely, τ_0 has a power spectral density (PSD) which is

$$\sqrt{P(k)} = \sqrt{1 \Bigg/ \left(1 + \left(\frac{k}{k_c}\right)^2\right)^{1+D}}, \qquad (21)$$

where $k = ||\mathbf{k}|| = \sqrt{k_1^2 + k_3^2}$, with k_1 and k_3 being the horizontal (along strike) and vertical (along depth) wave numbers, respectively. In (21) k_c is the radial wave number corresponding to the correlation length L_c ($k_c = 2\pi/L_c$), and D is the dimensionless Hurst exponent [see *Mai and Beroza*, 2002]. In equation (21) we choose D = 0, which corresponds in the static limit to the well-known "k-square"

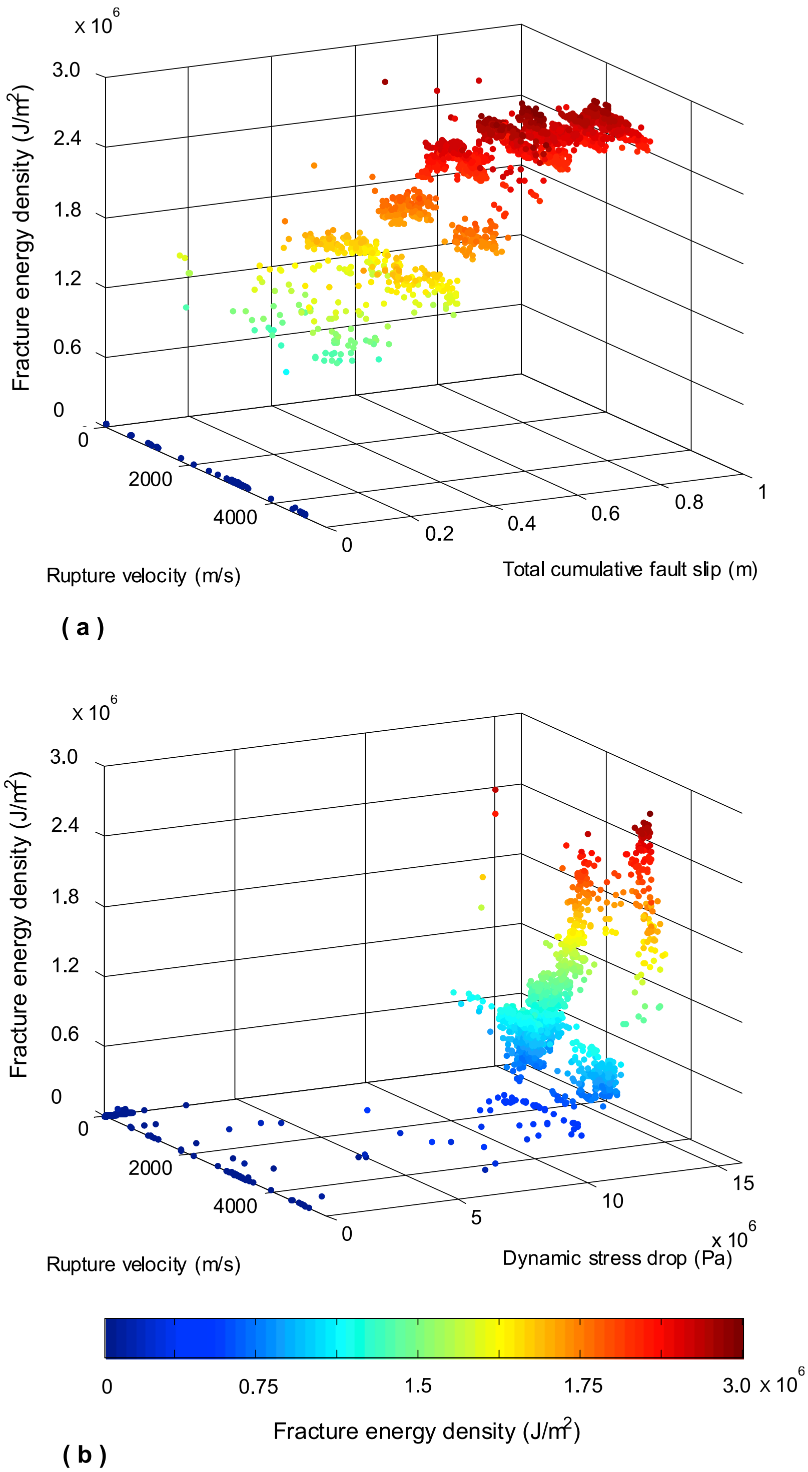

Figure 9. The same as in Figure 5, but now for the RD model reported in Figure 8, with $a = 0.012$ and $b = 0.020$.

Figure 10. (a) Magnitude of the initial shear stress adopted in heterogeneous simulations; the fluctuations with respect to the reference value of τ_0 listed in Table 1 (green color) follow the desired power spectral density (see section 7 for details). (b) Resulting Fourier amplitude spectra as a function of the radial wave number k; the dashed red curve emphasizes the required k^{-1} behavior. (c) Distribution of rupture velocity on the fault plane in the case of classical RD law. (d) Same as Figure 10c, but in the case of the SW law.

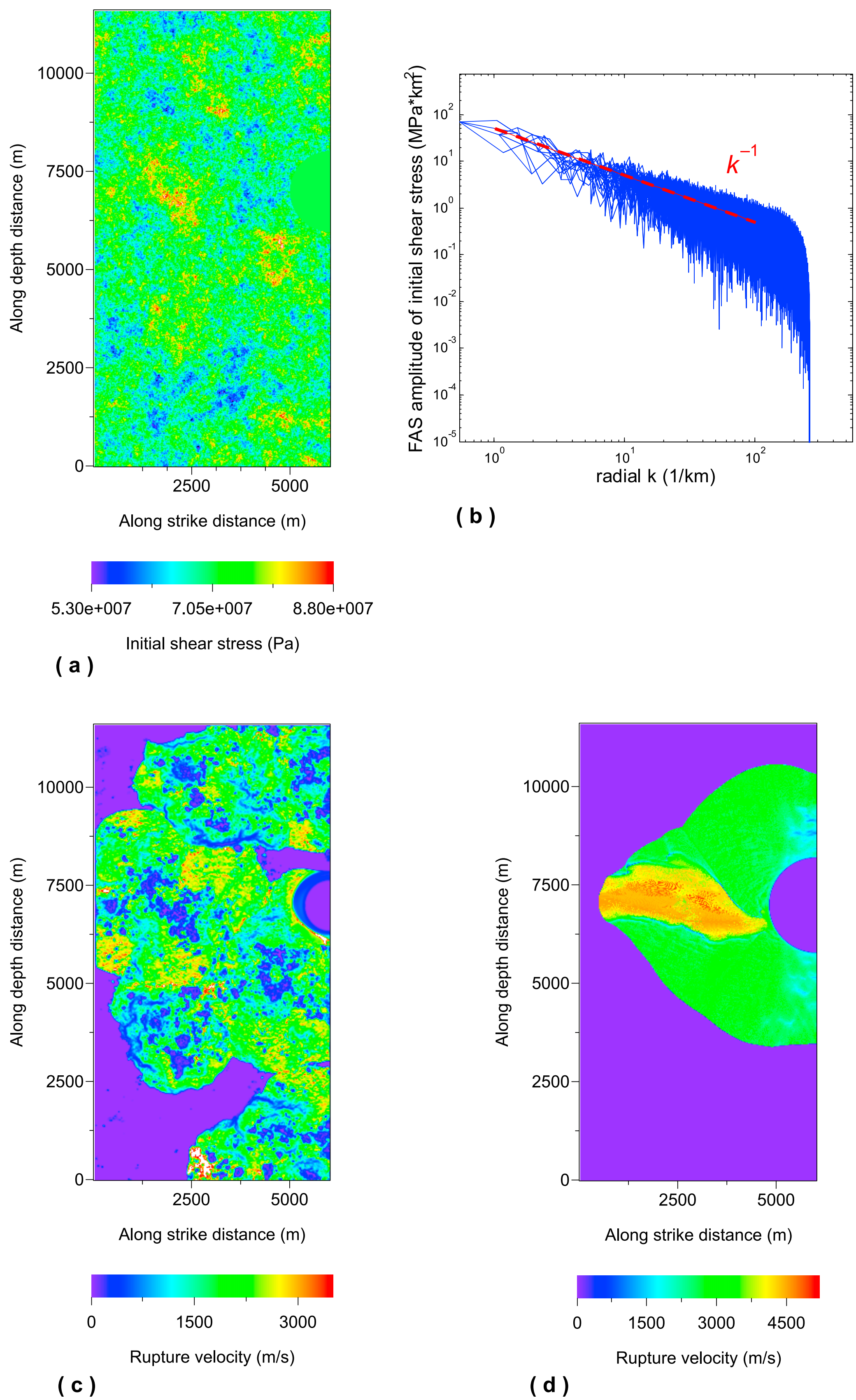

Along depth distance (m)
Along strike distance (m)
Initial shear stress (Pa)
5.30e+007
7.05e+007
8.80e+007
(a)
FAS amplitude of initial shear stress (MPa*km²)
radial k (1/km)
k⁻¹
(b)
Rupture velocity (m/s)
(c)
(d)

Figure 10

model [*Herrero and Bernard*, 1994] of slip at high wave numbers, corroborated by several inversions of ground motion data. We also set L_c = 1000 km in order to have a power law spectrum of the initial shear stress for all modelled wavelengths.

[35] The distribution of the initial shear stress adopted in the heterogeneous numerical experiments is reported in Figure 10a, where the green color identifies the reference value of τ_0, reported in Table 1. The resulting one dimension (1D) spectrum is plotted in Figure 10b, from which we can see that its PSD behaves like k^{-1}, as desired (dashed red curve); the RMS of such a distribution is 5.52 MPa. We apply the heterogeneous stress of Figure 10a in two numerical experiments, one with the classical RD law (equation (19)) and the other one with the SW law (equation (18)). In the latter case, the heterogeneities in τ_0 will affect rupture times, rupture velocity, and total cumulative slip, but when τ_u, τ_f, and d_0 are spatially homogeneous, the resulting E_G will be constant (see equation (2)), as in a homogenous simulation. Therefore, to allow for a variable E_G in the SW case, we also add heterogeneities in τ_u, which is spatially variable, such that the strength excess $\tau_u - \tau_0$ is constant (and equal to the reference value of the homogeneous configuration reported in Table 1). The other constitutive parameters are those tabulated in Table 1.

[36] The two resulting models behave very differently; this is clear from the comparison of Figures 10c and 10d, where we report the distribution of v_r on the fault plane. On the basis of the fluctuations of τ_0, in the RD case there are multiple points on the fault where the rupture starts to propagate dynamically. This behavior is similar to that obtained by *Bizzarri and Spudich* [2008, Figure 11]; the multiple ruptures interact with one another and insert a further complication into the model, other than the imposed heterogeneity of τ_0. On the contrary, the SW simulation exhibits a more usual behavior; rupture initiates within the nucleation patch and then propagates dynamically. In both cases, the presence of heterogeneities complicates the evolution of the rupture front and furthermore it causes, especially in the SW model, local acceleration to supershear rupture speeds. In these two models, both subshear and supershear rupture patches exist. Correspondently, the distributions on the fault plane of u_{tot} and E_G are quite different between two simulations (compare Figure 11a with Figure 11b and Figure 11c with Figure 11d).

[37] We report in Figure 12 the resulting behavior of E_G as a function of rupture velocity (Figure 12a), total cumulative fault slip (Figure 12b), and dynamic stress drop (Figure 12c). We can clearly see that E_G exhibits large fluctuations due to frictional heterogeneities. In this case it is hard to find a clear and well-defined trend of E_G as a function of v_r. We can also see that in the RD model E_G increases roughly linearly for increasing u_{tot} (Figure 12b, red symbols), as previously observed in the homogeneous sustained supershear RD simulations (Figures 8b and 9a). In the SW case, E_G does not have a strong dependence on u_{tot} (Figure 12b, blue symbols); it is oscillating above and below a constant value, slightly greater to the reference value of fracture energy density pertaining to the homogeneous configurations (equation (2)). Large fluctuations are also present in the E_G versus $\Delta\tau_d$ curve (Figure 12c), which indicate a linear increase of E_G for increasing $\Delta\tau_d$.

8. Discussion

[38] In previous sections, we have reported the results of different numerical simulations that are representative of different fault governing laws, rupture regimes, and initial conditions. We have considered a grid-by-grid analysis to show the behavior of fracture energy density as a function of physical observables. In this section, we summarize results of a different kind of analysis, which is performed by considering event by event. In particular, we take into account the whole ensemble of simulations, comprised of 40 numerical experiments of fully dynamic and spontaneous seismic ruptures that cover a broad magnitude range (M_0 from 4.25×10^{17} Nm up to 1.07×10^{19} Nm; corresponding to M_w from 5.8 to 6.7). For each synthetic event we consider the spatial averages, over the fault nodes experiencing the rupture, of E_G, v_r, u_{tot}, and $\Delta\tau_d$ (in the following we denote them with symbols $\langle E_G\rangle$, $\langle v_r\rangle$, $\langle u_{tot}\rangle$, and $\langle\Delta\tau_d\rangle$, respectively.) The results are shown in Figure 13. First of all, we emphasize that it is impossible to compare data against a single curve, exactly representing the theoretical predictions discussed in section 2, because they contain quantities that cannot be spatially averaged. For example, in equations (11) and (13) the quantity r denotes the distance of a rupturing fault node from the hypocenter H, a quantity which cannot spatially averaged. On the other hand, L_{pulse} is equation (7) depends on the specific rupture we consider; thus, that multiplier factor is different from one event to another.

[39] A first observation coming from Figure 13 is that the results are quite sparse; this is not surprising, given the broad range of input parameters. On the other hand, the values estimated by kinematic inversion for different real earthquakes [*Tinti et al.*, 2005; see also *Abercrombie and Rice*, 2005], represented by shaded triangles in Figure 13, also appear to be quite sparse.

[40] From Figure 13a we can see that, for subshear ruptures (open symbols), E_G behaves roughly like $\sqrt{1-\left(v_r^2/v_S^2\right)}$ (black curve in Figure 13a), as previously observed (Figure 4a). On the contrary, for supershear synthetic events (full symbols), data appear to be clustered around a value of $\langle v_r\rangle$ nearly equal to Eshelby's speed ($v_E = \sqrt{2}\ v_S$), but there is a large variability of $\langle E_G\rangle$. In this rupture regime it is difficult to find a specific behavior of fracture energy density as a function of rupture velocity, in agreement with results previously discussed (see Figures 6a, 7b, 8, and 9b). It is apparent from Figure 13b that our results seem to agree better as a linear fit with $\langle u_{\text{tot}}\rangle$, as suggested by *McGarr et al.* [2004] (green curve in Figure 13b). This also confirms what we have observed in Figures 8b and 9a for a cracklike rupture. From Figure 13c we can see that $\langle E_G\rangle$ roughly goes like $\langle\Delta\tau_d\rangle^{\alpha}$, where α is in between 1 and 2, as also found above (see Figures 4b and 12c). The only exception is represented by the sustained supershear FH pulses (group of pink diamonds on the right), that have extremely high dynamic stress drop (55 MPa for the case reported in Figures 6c and 7b).

[41] We have also checked if two parameters quantifying a faulting episode as a whole, the total fracture energy (U_G; see equation (5)) and the scalar seismic moment (M_0), cor-

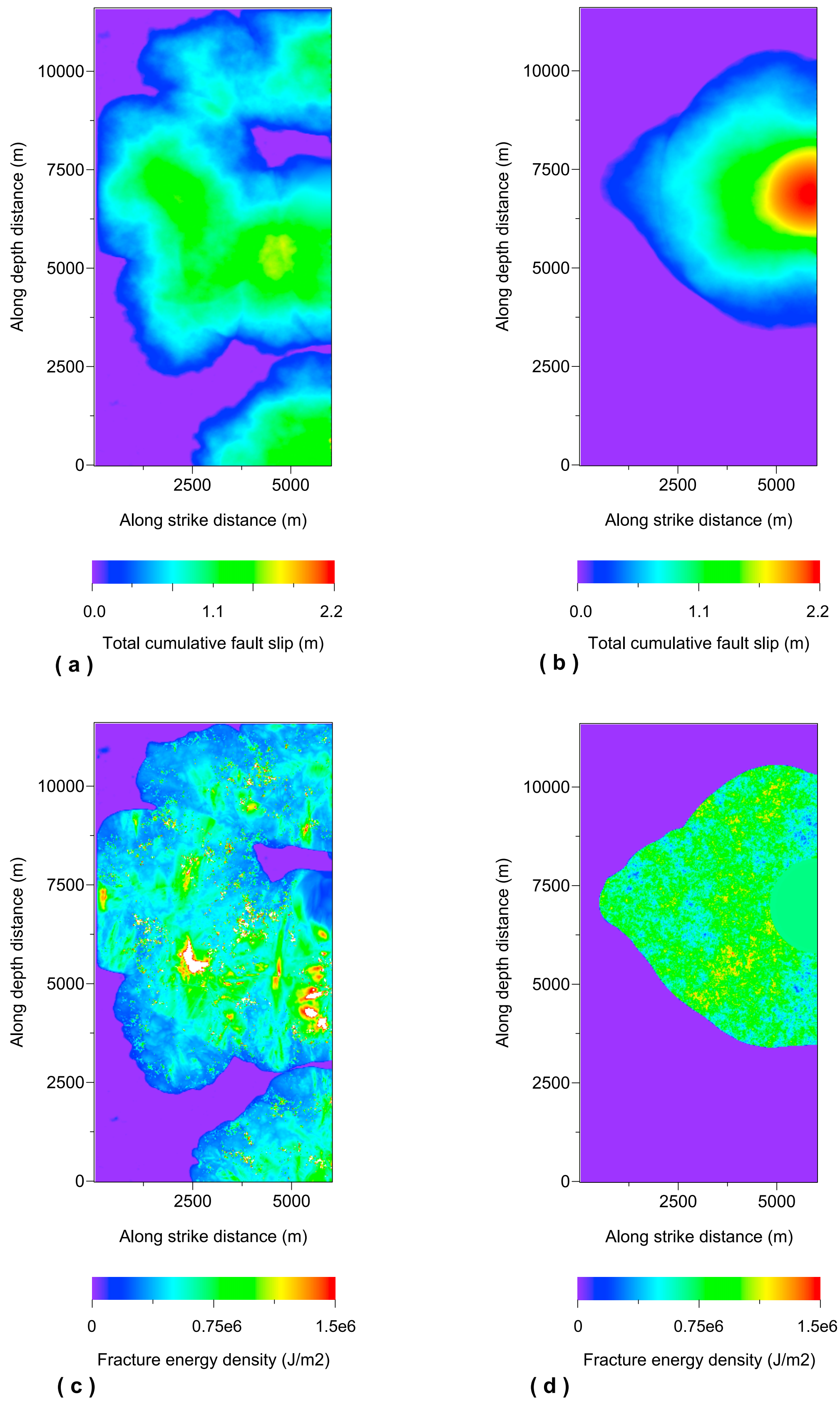

Figure 11. Distribution on the fault plane of (top) u_{tot} and (bottom) E_G pertaining to the heterogeneous rupture of (left) Figure 10c and (right) Figure 10d.

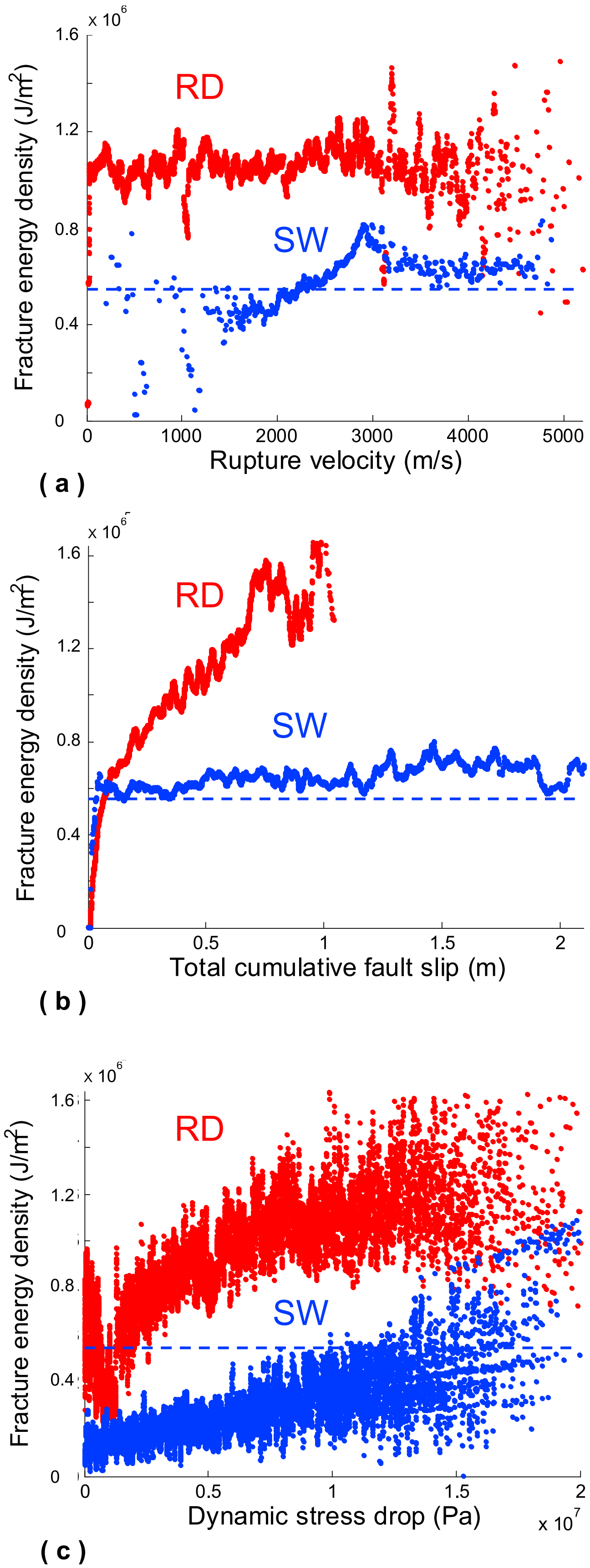

Figure 12. Results for heterogeneous configurations of Figures 10 and 11; red symbols refer to RD model and blue symbols refer to the SW model. (a) E_G as a function of v_r. (b) E_G as a function of u_{tot}. (c) E_G as a function of $\Delta\tau_d$. The dashed blue curve indicates the reference value of E_G for the homogeneous SW model, as given by equation (2).

relate. In Figure 14 we report the values of U_G and M_0 for the whole ensemble of synthetic earthquakes, obeying different constitutive laws and for homogeneous (squares) and heterogeneous (circles) conditions. We notice that these values refer to the rupture developed over the whole fault of length L^f = 12 km; since the rupture is bilateral and symmetric with respect to the hypocenter we simply double the values obtained for the fault considered for computations, which extends only 6 km. In Figure 14 we have also superimposed, as shaded triangles, the values estimated from kinematic inversions by *Tinti et al.* [2005] for several real events. We can clearly see that our dynamic models exhibit a power law relationship between total fracture energy and scalar seismic moment, with a slope that depends very weakly on the inclusion of the fault points within the nucleation patch. In fact, full symbols (for which U_G and M_0 are determined for all fault points) and open symbols (for which nodes within I_{nucl} are not considered in the calculation of U_G and M_0) indicate slopes of 1.13 and 1.14, respectively (solid and dashed red curves in Figure 14, respectively). This power law exponent is in agreement with the value of 1.18 estimated in the kinematic models of *Tinti et al.* [2005] (shaded curve). For comparison we also plot in Figure 14 the power law found by *Abercrombie and Rice* [2005] (see equation (15)), having an exponent q = 1.28 (black curve).

9. Conclusions

[42] In addition to the amount of dissipation occurring during healing process [*Broberg*, 1978], the fracture energy density (E_G) is one of the key parameters in the physics of the earthquake source [e.g., *Kostrov*, 1964]. Compared to other source parameters, E_G has been proved to be more stably estimated from kinematic rupture models inferred from waveform inversions of strong motion data [*Guatteri and Spudich*, 2000] and has an important influence in discriminating between melting and nonmelting regimes [*Bizzarri*, 2010b]. The basic objective of the present paper is to see if E_G exhibits some specific dependencies on the most prominent physical quantities (observables or dynamic variables), such as the rupture velocity (v_r), the total cumulative fault slip (u_{tot}) and the dynamic stress drop ($\Delta\tau_d$). This has been done for scenarios more realistic and more complex than (necessarily) simplified models for which some prediction has been derived theoretically.

[43] In general, to accurately predict ground motions by a kinematic numerical model and for simulation-based seismic hazard analysis, it is necessary not only to know the spatial distribution of the source parameters, but also to know the correlations among them [e.g., *Song et al.*, 2009; *Schmedes et al.*, 2010].

[44] To explore these relationships we have performed 40 numerical simulations of fully dynamic and spontane-

ous seismic ruptures that cover a wide size range (M_0 from 4.25×10^{17} Nm to 1.07×10^{19} Nm, corresponding to M_w from 5.8 to 6.7) and span a broad range of relevant situations. The synthetic earthquakes are 3D ruptures (with rake rotation allowed and a possible continuous transition from sub to supershear regimes) and develop on a planar fault of finite size, which is governed by different constitutive laws, the linear slip-weakening (SW) function (equation (18)), the Ruina-Dieterich (RD) form of rate- and state-dependent laws (equation (19)), and the RD law

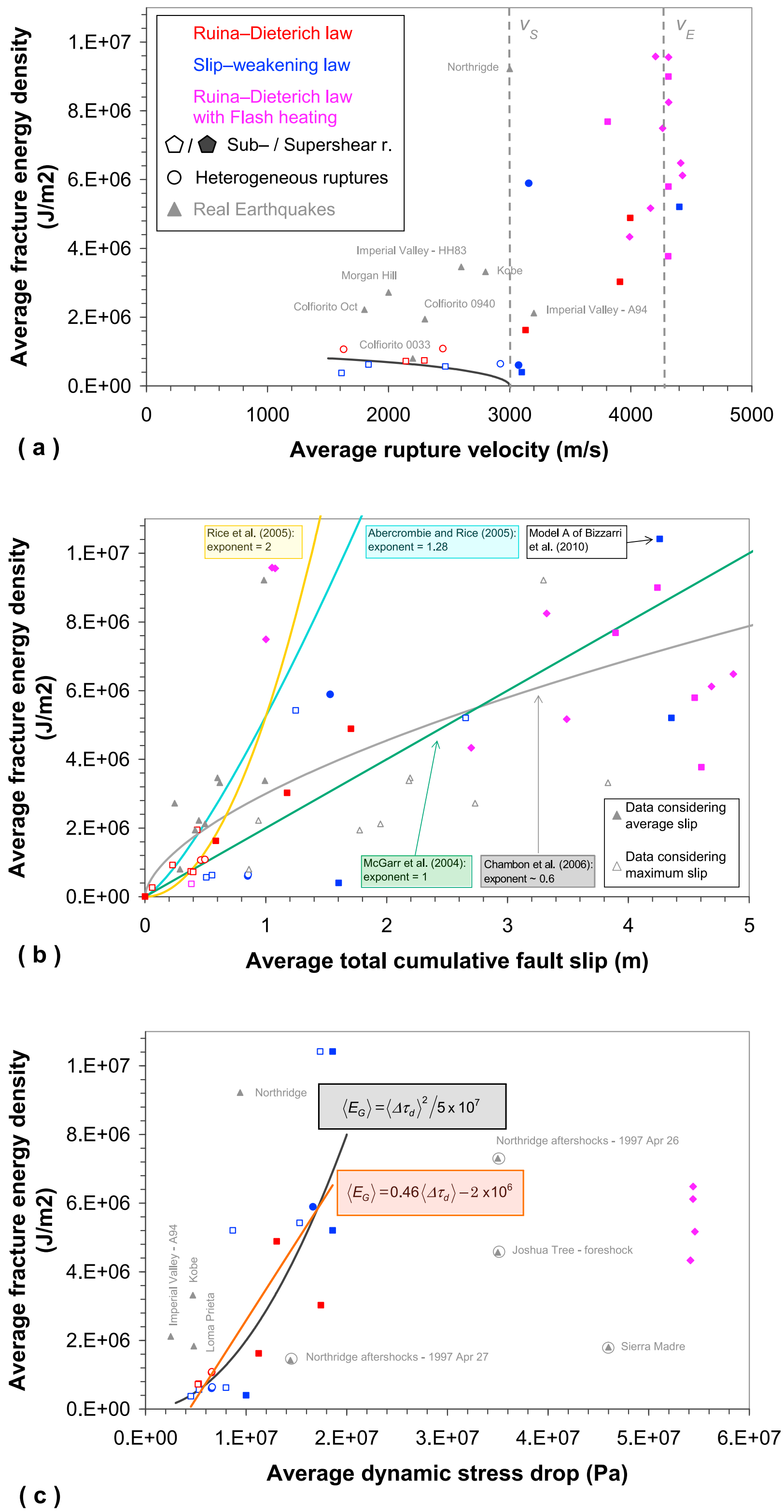

Figure 13

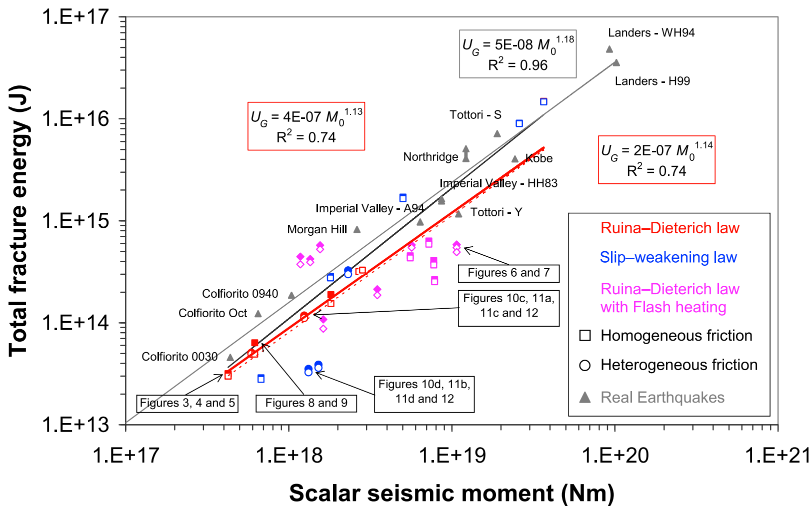

Figure 14. Relation between total fracture energy U_G, calculated from equation (5), and scalar seismic moment M_0 calculated as described by *Bizzarri and Belardinelli* [2008]. Full symbols denote the calculations of U_G where points within the nucleation patch are considered; open symbols denote the estimates of U_G obtained neglecting points within I_{nucl}. Solid and dashed red curves are the fits on synthetic data (as including and neglecting points within I_{nucl}, respectively). For comparison we report the power law by *Tinti et al.* [2005] (shaded curve, with exponent of M_0 equal to 1.18) and that found by *Abercrombie and Rice* [2005] (black curve, with exponent of M_0 equal to 1.28).

accounting for flash heating (FH) of asperity contacts (equation (20)). We have considered both homogeneous and heterogeneous distributions of the initial shear stress on the fault, and both subshear and supershear rupture events. Overall, by taking into account all the ruptures in our synthetic catalog, we have examined about 44 million fault points.

[45] All of our earthquake models exhibit a well defined residual friction that is approached at large slips and therefore the fracture energy density can be precisely computed by using equation (1); incidentally, we emphasize that in the opposite case E_G would not be a precisely defined concept. The fracture energy density E_G can be regarded as mesoscopic [see also *Mai et al.*, 2006], comprising surface energy, energy loss due to off-fault yielding, micro-cracking, frictional heat, and all other dissipative processes occurring in the rock volume surrounding the rupture tip. An increase in energy flux at the tip of a propagating rupture is responsible for an increase in the number of coalescent microvoids and microcracks [*Sharon et al.*, 1996].

[46] In the literature different analytical relations have been reported, but they intrinsically suffer some limitations in basic assumptions (namely, they have been derived for rupture velocities not greater than S wave speed and in the case of simple 2D ruptures). On the other hand, presently available kinematic inversions of strong motion data do not give clear indication of the dependences of E_G on observables; thus, dynamic models can help us in filling this gap. Moreover, it is well known that fracture energy density from laboratory experiments are 3–5 orders of magnitude smaller than that inferred for earthquakes [e.g., *Rudnicki*, 1980], making it difficult to extrapolate laboratory results to natural conditions. As a consequence, physics-based earthquake source models represent a powerful tool to explore more general, and potentially more realistic, physical scenarios.

[47] We can summarize the results we obtain from our numerical experiments as follows.

[48] 1. As is well-known, in homogeneous conditions the linear SW law gives a constant value of E_G, which is uniform on the whole fault plane and is independent on physical observables. For a single event, the comparison with the theoretical predictions is inherently impossible in this case; for instance, E_G generally is a non-unique function of v_r. On

Figure 13. Results from the event-by-event analysis; the quantities E_G, v_r, u_{tot}, and $\Delta\tau_d$ are spatially averaged, for each event, over the points that fail. Red symbols refer to numerical experiments in which classical RD law is adopted, blue symbols refer to SW models, and pink symbols refer to FH simulations. Circles refer to models with heterogeneous conditions; diamonds indicate pulselike solutions. Open and full symbols denote sub- and supershear ruptures, respectively. For comparison we also add, as shaded triangles, the estimates obtained from kinematic inferences for some real earthquakes by *Tinti et al.* [2005] (reader can refer to that work for references about source models). $\langle E_G \rangle$ as a function of (a) $\langle v_r \rangle$, (b) $\langle u_{\mathrm{tot}} \rangle$, and (c) $\langle \Delta\tau_d \rangle$. In Figure 13a the black curve reproduces the behavior $\sim \sqrt{1-\left(v_r^2/v_S^2\right)}$. In Figure 13b we report different fits from the literature (various exponents of u_{tot} are indicated in the legends). In Figure 13c the triangles surrounded by a circle are extracted from the works by *Abercrombie and Rice* [2005, Table 5, and references therein], by using the relation $E_G = (1/2\pi R^2)[(\Delta\tau_d M_0/G) - E_S]$, where R is the source radius and E_S is the radiated energy.

the other hand, by considering different events, with homogeneous constitutive parameters, E_G can also be a non-unique function of $\Delta\tau_d$ (for fixed values of τ_u, τ_f and d_0, different values of τ_0 give different $\Delta\tau_d$ corresponding to the same value of E_G).

[49] 2. Subshear, homogeneous ruptures governed by RD law show a general agreement with the theoretical prediction (equation (13)) of $E_G \propto \sqrt{1 - \left(v_r^2/v_S^2\right)}$ (see Figures 4a and 13a).

[50] 3. On the contrary, for ruptures that accelerate up to supershear speeds it is extremely difficult to infer a clear dependence of fracture energy density on rupture speed (see Figures 6a, 8a, and 13b). Homogeneous simulations with RD law roughly indicate that E_G seems to be a concave function of v_r (see Figure 8a), in general agreement with the results obtained by *Bhat et al.* [2007] in 2D. However, the introduction of frictional heterogeneities further complicates this behavior and add some fluctuations to E_G so that there is no an apparent dependence of E_G on v_r (see Figure 12a). The existence of a relationship between E_G and v_r is intriguing and several physical motivations have been proposed to justify it (see *Sharon et al.* [1996] for a discussion), but we want to emphasize here that, especially for small earthquakes, there are some limitations in making estimates of the local rupture velocity of a real-world earthquake from the inversion of seismic waves. Moreover, the results can be non-unique. On the other hand, by considering a purely mode II crack growing on a granite sample, *Ohnaka et al.* [1987, equation (5)] found an empirical relation relating the peak slip velocity on the rupture plane, v_{peak}, v_r, and $\Delta\tau_b$,

$$v_r \cong v_{\text{peak}} \frac{G}{\Delta\tau_b}, \tag{22}$$

which gives (once substituted into equation (7) and equations (11–13)) an implicit dependence of E_G on v_{peak}. Equation (22) makes sense, since particle velocity and ground motions are determined by the rupture speed and this reinforces the fact that the fracture energy density is arguably one of the most important physical property in the earthquake source models. A strong correlation between v_{peak} and v_r has been also confirmed by the dynamic subshear numerical simulations of *Schmedes et al.* [2008].

[51] 4. On average, the spatial distributions on the fault surface of fracture energy density are correlated with the corresponding slip distributions (see Figure 11); high slip patches correspond to high E_G, in general agreement with the kinematic findings of *Tinti et al.* [2005]. This correlation is primarily due to the correlation of characteristic slip-weakening distance with slip, but also to the correlation of $\Delta\tau_b$ with u_{tot}. More specifically, our results in 3D confirm that slip pulses noticeably exhibit a behavior like $E_G \propto u_{\text{tot}}^2$ (Figures 6b and 7a), as predicted by the theory for 2D steady pulses (see equation (7)). On the contrary, in the cases of cracklike solutions, both sub- and supershear and both homogeneous and heterogeneous, this behavior is not confirmed by spontaneous, dynamic rupture models (see Figures 4b, 8a, and 12b). Our results (see Figure 13b) are in better agreement with the seismological inferences of *McGarr et al.* [2004] and results of dynamic rupture models of *Mai et al.* [2006, equation (5)], from which it emerges as a scaling exponent roughly equal to 1.

[52] 5. The proportionality between E_G and $\Delta\tau_d^2$ expected from the theoretical predictions (see equations (11–13)) is somewhat verified in homogeneous, subshear ruptures with RD law (Figures 4c and 5b). On the contrary, in the cases of supershear rupture obeying the RD law (Figures 8c and 9b), and heterogeneous events (Figure 12c) our numerical experiments roughly suggest $E_G \propto \Delta\tau_d$ (see also Figure 13c). We want to remark that in the present simulations we neglected variability with depth of the effective normal stress, which would introduce a depth-dependence of stress drop.

[53] 6. Our spontaneous rupture models indicate that the total fracture energy (U_G; equation (5)) and the scalar seismic moment (M_0) correlate, with a power law dependence with an exponent equal to 1.13 (Figure 14), according to previous studies [e.g., *Tinti et al.*, 2005].

[54] Overall, we notice that the values of the fracture energy density obtained in our dynamic models are comparable with values reported in previous studies [see *Guatteri and Spudich*, 2000; *McGarr et al.*, 2004 for a review]; we emphasize here that seismological estimates ($E_G \sim 10^5$ to 10^7 J/m^2) can be an overestimate due to low-pass filtering of the seismograms [*Spudich and Guatteri*, 2004].

[55] To finish, the dependences of the fracture energy density on rupture velocity, on cumulative fault slip, and on dynamic stress drop as discussed above depend on the adopted governing equation (the choice of which is still matter of a lively debate [e.g., *Bizzarri and Cocco*, 2006b] and, what is more, on the rupture regime (cracklike or pulselike; as well as sub- or supershear speed). Moreover, these dependencies appear to be in favor of the idea [see also *Okubo and Dieterich*, 1986; *Abercrombie and Rice*, 2005] that E_G should not be regarded as an intrinsic material parameter.

Appendix A: Effects of the Nonzero-Offset Correlation Analysis

[56] In the grid-by-grid analysis presented in sections 5–7 we have considered a zero-offset distance correlation analysis. In other words, we have considered the value of the fracture energy density and of the other physical quantities in the same fault node. Here, we consider a nonzero-offset distance correlation, in which the observables are defined in different points of the fault plane.

[57] Let us consider two spatially distributed 2D arrays, $X \equiv \{x_{i,k}\}$ and $Y \equiv \{y_{i,k}\}$ (with i = 1, .., i_{end} and k = 1, .., k_{end}), characterized by their average values, $\langle X \rangle$ and $\langle Y \rangle$, respectively, and by their standard deviations, σ_X and σ_Y, respectively. We will consider the normalized covariance between them, C, defined as [e.g., *Goovaerts*, 1997]

$$C = \frac{E\left(\left(X - \langle X \rangle\right)\left(\tilde{Y} - \langle Y \rangle\right)\right)}{\sigma_X \sigma_Y}, \tag{A1}$$

where $E(.)$ is the expected value operator and $\tilde{Y}$ denotes the array Y translated by a vector $\mathbf{h} \equiv ((\alpha - 1)\Delta x_1, (\beta - 1)\Delta x_3) = ((\alpha - 1), (\beta - 1))\Delta x$. More specifically, we compute C of (A1) as

$$C_{\alpha,\beta} = \frac{\sum_{i=1}^{i_{\text{end}}-\alpha+1} \sum_{k=1}^{k_{\text{end}}-\beta+1} \left(x_{i,k} - \langle X \rangle\right)\left(y_{i+\alpha-1,k+\beta-1} - \langle Y \rangle\right)}{(i_{\text{end}} - \alpha + 1)(k_{\text{end}} - \beta + 1)\sigma_X \sigma_Y} \tag{A2}$$

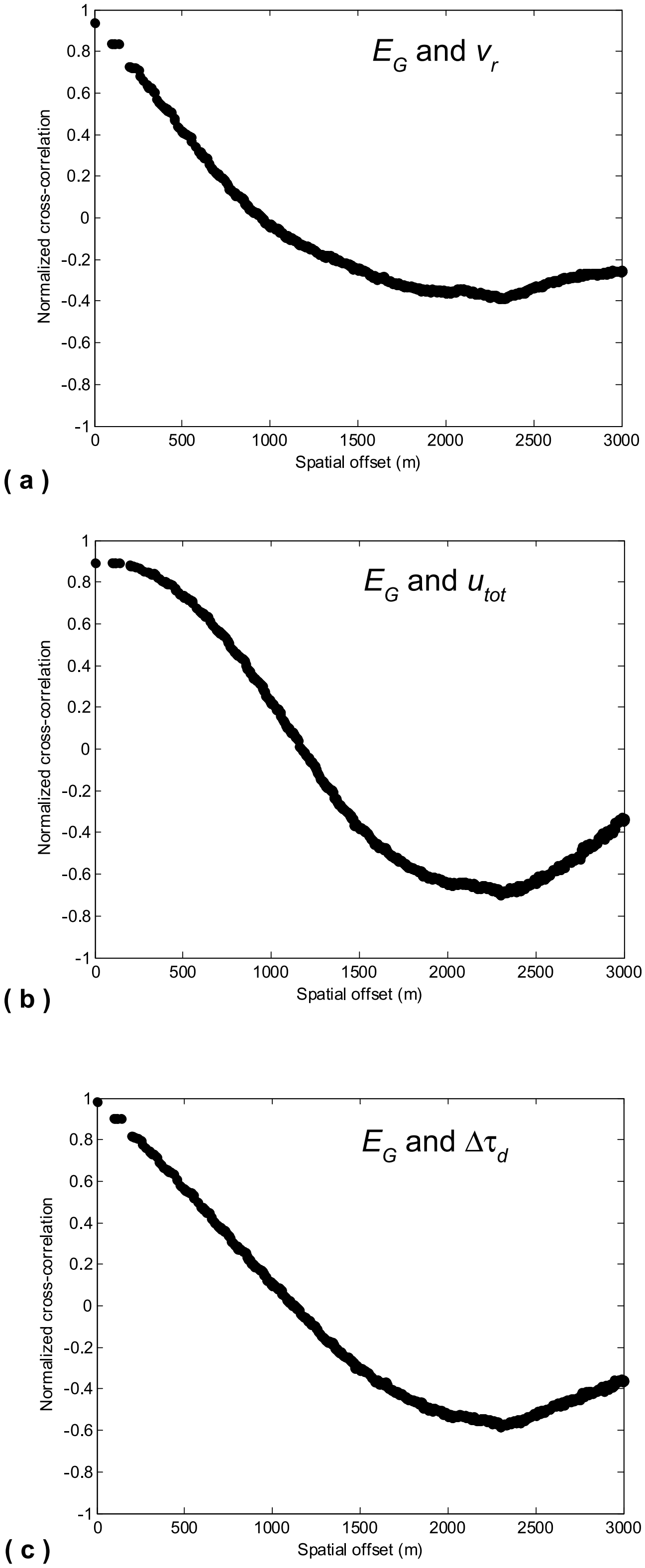

Figure A1. Results of the nonzero-offset distance analysis for the model reported in Figures 3, 4, and 5. The normalized cross-correlation, calculated as in equation (A2), is reported as a function of spatial offset between fracture energy density and (a) rupture velocity, (b) total cumulative fault slip, and (c) dynamic stress drop.

with $\langle X \rangle = \frac{1}{i_{\text{end}} k_{\text{end}}} \sum_{i=1}^{i_{\text{end}}} \sum_{k=1}^{k_{\text{end}}} x_{i,k}$ and $\sigma_X = \sqrt{\frac{1}{i_{end} k_{end}} \sum_{i=1}^{i_{\text{end}}} \sum_{k=1}^{k_{\text{end}}} \left(x_{i,k} - \langle X \rangle \right)^2}$ (and analogous expressions for Y). The translation vector $\mathbf{h}$ defines a spatial offset distance $h = \sqrt{(\alpha - 1)^2 + (\beta - 1)^2}\, \Delta x$ and an azimuth angle $\varphi = \arctan\,(\beta - 1)/(\alpha - 1))$.

[58] The pair $(\alpha, \beta) = (1, 1)$ corresponds to a zero-offset distance, so that $C_{\alpha,\beta}$ becomes the autocorrelation function ($A = E((X - \langle X \rangle)\,(Y - \langle Y \rangle))/\sigma_X \sigma_Y$). The $C_{\alpha,\beta}$, which is also known as a correlogram [*Goovaerts*, 1997], represents the linear dependency between the two variables X and Y, and it varies between -1 and 1 [see also *Song et al.*, 2009]. The evaluation of $C_{\alpha,\beta}$ for different values of h (i.e., for different values of α and β) enables us to quantify the potential spatial coherence between spatially varying variables X and Y.

[59] For the present purposes, we associate X to E_G and Y alternatively to v_r, u_{tot}, and $\Delta\tau_d$. Results pertaining to the model reported in Figures 3, 4, and 5 are plotted in Figure A1, where values of $C_{\alpha,\beta}$ corresponding to the same value of spatial offset distance h are averaged [see *Bizzarri et al.*, 2010, Figure 11b]. We can clearly see that maximum spatial correlation exists at the zero-offset distance for all of the physical observables, v_r (Figure A1a), u_{tot} (Figure A1b), and $\Delta\tau_d$ (Figure A1c). For increasing spatial offset $C_{\alpha,\beta}$ decreases reaching a minimum for a value of h nearly equal to 2.3 km. This behavior recalls that obtained by *Song et al.* [2009, Figure 4], that relates slip to peak slip velocity and rise time. The slopes of the three curves reported in Figure A1 are slightly different, with a roll-off in the case of slip (Figure A1b).

[60] The maximum spatial correlation existing at zero-offset distance corroborates the same point, grid-by-grid analysis presented in sections 5 to 7.

[61] **Acknowledgments.** P. Spudich is kindly acknowledged for a thorough, preliminary review of the paper. I am grateful to the editor, R. Nowack; to the associate editor; to S. G. Song and J. Fletcher; and to an anonymous referee for their stimulating comments that improved the paper.

References

Abercrombie, R. E., and J. R. Rice (2005), Can observations of earthquake scaling constrain slip weakening?, *Geophys. J. Int.*, *162*, 406–424, doi:10.1111/j.1365-246X.2005.02579.x.

Aki, K. (1967), Scaling law of seismic spectrum, *J. Geophys. Res.*, *72*, 1217–1231, doi:10.1029/JZ072i004p01217.

Aki, K., and P. G. Richards (2002), *Quantitative Seismology*, 2nd ed., 700 pp., Univ. Sci. Books, Sausalito, Calif.

Andrews, D. J. (1976a), Rupture propagation with finite stress in antiplane strain, *J. Geophys. Res.*, *81*, 3575–3582, doi:10.1029/JB081i020p03575.

Andrews, D. J. (1976b), Rupture velocity of plane strain shear cracks, *J. Geophys. Res.*, *81*, 5679–5687, doi:10.1029/JB081i032p05679.

Andrews, D. J. (2005), Rupture dynamics with energy loss outside the slip zone, *J. Geophys. Res.*, *110*, B01307, doi:10.1029/2004JB003191.

Bhat, H. S., R. Dmowska, G. C. P. King, Y. Klinger, and J. R. Rice (2007), Off-fault damage patterns due to supershear ruptures with application to the 2001 M_w 8.1 Kokoxili (Kunlun) Tibet earthquake, *J. Geophys. Res.*, *112*, B06301, doi:10.1029/2006JB004425.

Bizzarri, A. (2009a), Can flash heating of asperity contacts prevent melting?, *Geophys. Res. Lett.*, *36*, L11304, doi:10.1029/2009GL037335.

Bizzarri, A. (2009b), What does control earthquake ruptures and dynamic faulting? A review of different competing mechanisms, *Pure Appl. Geophys.*, *166*, 741–776, doi:10.1007/s00024-009-0494-1.

Bizzarri, A. (2010a), How to promote earthquake ruptures: Different nucleation strategies in a dynamic model with slip-weakening friction, *Bull. Seismol. Soc. Am.*, *100*, 923–940, doi:10.1785/0120090179.

Bizzarri, A. (2010b), An efficient mechanism to avert frictional melts during seismic ruptures, *Earth Planet. Sci. Lett.*, *296*, 144–152, doi:10.1016/j.epsl.2010.05.012

Bizzarri, A., and M. E. Belardinelli (2008), Modelling instantaneous dynamic triggering in a 3-D fault system: Application to the 2000 June South Iceland seismic sequence, *Geophys. J. Int.*, *173*, 906–921, doi:10.1111/j.1365–246X.2008.03765.x.

Bizzarri, A., and M. Cocco (2003), Slip-weakening behavior during the propagation of dynamic ruptures obeying rate- and state-dependent friction laws, *J. Geophys. Res.*, *108*(B8), 2373, doi:10.1029/2002JB002198.

Bizzarri, A., and M. Cocco (2005), 3D dynamic simulations of spontaneous rupture propagation governed by different constitutive laws with rake rotation allowed, *Ann. Geophys.*, *48*(2), 279–299.

Bizzarri, A., and M. Cocco (2006a), A thermal pressurization model for the spontaneous dynamic rupture propagation on a three-dimensional fault: 2. Traction evolution and dynamic parameters, *J. Geophys. Res.*, *111*, B05304, doi:10.1029/2005JB003864.

Bizzarri, A., and M. Cocco (2006b), Comment on "Earthquake cycles and physical modeling of the process leading up to a large earthquake," *Earth Planets Space*, *58*, 1525–1528.

Bizzarri, A., and P. Spudich (2008), Effects of supershear rupture speed on the high-frequency content of *S* waves investigated using spontaneous dynamic rupture models and isochrone theory, *J. Geophys. Res.*, *113*, B05304, doi:10.1029/2007JB005146.

Bizzarri, A., M. Cocco, D. J. Andrews, and E. Boschi (2001), Solving the dynamic rupture problem with different numerical approaches and constitutive laws, *Geophys. J. Int.*, *144*, 656–678, doi:10.1046/j.1365-246x.2001.01363.x.

Bizzarri, A., E. M. Dunham, and P. Spudich (2010), Coherence of Mach fronts during heterogeneous supershear earthquake rupture propagation: Simulations and comparison with observations, *J. Geophys. Res.*, *115*, B08301, doi:10.1029/2009JB006819.

Broberg, K. B. (1978), On the transient sliding motion, *Geophys. J. R. Astron. Soc.*, *52*, 297–432.

Broberg, K. B. (1999), *Cracks and Fracture*, 752 pp., Academic, London.

Brown, S. R. (1998), Frictional heating on faults: Stable sliding versus stick slip, *J. Geophys. Res.*, *103*, 7413–7420, doi:10.1029/98JB00200.

Burridge, R. (1973), Admissible speeds for plane-strain self-similar shear cracks with friction but lacking cohesion, *Geophys. J. R. Astron. Soc.*, *35*, 439-455.

Chambon, G., J. Schmittbuhl, and A. Corfdir (2006), Frictional response of a thick gouge sample: 2. Friction law and implications for faults, *J. Geophys. Res.*, *111*, B09309, doi:10.1029/2004JB003339.

Chester, J. S., F. M. Chester, and A. K. Kronenberg (2005), Fracture surface energy of the Punchbowl fault, San Andreas system, *Nature*, *437*, 133–136, doi:10.1038/nature03942.

Cocco, M., and A. Bizzarri (2002), On the slip-weakening behavior of rate- and state dependent constitutive laws, *Geophys. Res. Lett.*, *29*(11), 1516, doi:10.1029/2001GL013999.

Cocco, M., P. Spudich, and E. Tinti (2006), On the mechanical work absorbed on faults during earthquake ruptures, in *Earthquakes: Radiated Energy and the Physics of Faulting*, *Geophys. Monogr. Ser.*, vol. 170, edited by R. Abercrombie et al., pp. 237–254, AGU, Washington, D. C.

Day, S. M. (1982), Three-dimensional finite difference simulation of fault dynamics: Rectangular faults with fixed rupture velocity, *Bull. Seismol. Soc. Am.*, *72*, 705–727.

Dunham, E. M., and H. S. Bhat (2008), Attenuation of radiated ground motion and stresses from three-dimensional supershear ruptures, *J. Geophys. Res.*, *113*, B08319, doi:10.1029/2007JB005182.

Freund, L. B. (1979), The mechanics of dynamic shear crack propagation, *J. Geophys. Res.*, *84*, 2199–2209, doi:10.1029/JB084iB05p02199.

Goovaerts, P. (1997), *Geostatistics for Natural Resources Evaluation*, *Oxford Univ. Press*, New York.

Guatteri, M., and P. Spudich (2000), What can strong-motion data tell us about slip-weakening fault-friction laws?, *Bull. Seismol. Soc. Am.*, *90*, 98-116, doi:10.1785/0119990053.

Haskell, N. (1964), Total energy and energy spectral density of elastic wave radiation from propagating faults, *Bull. Seismol. Soc. Am.*, *56*, 1811–1842.

Herrero, A., and P. Bernard (1994), A kinematic self-similar rupture process for earthquakes, *Bull. Seismol. Soc. Am.*, *84*, 1216–1228.

Husseini, M. I., and M. J. Randall (1976), Rupture velocity and radiation efficiency, *Bull. Seismol. Soc. Am.*, *66*, 1173–1187.

Husseini, M. I., D. B. Jovanovich, M. J. Randall, and L. B. Freund (1975), The fracture energy of earthquakes, *Geophys. J. R. Astron. Soc.*, *43*, 367–385.

Ida, Y. (1972), Cohesive force across the tip of a longitudinal-shear crack and Griffith's specific surface energy, *J. Geophys. Res.*, *77*, 3796–3805.

Ionescu, I. R., and M. Campillo (1999), Influence of the shape of the friction law and fault finiteness on the duration of initiation, *J. Geophys. Res.*, *104*, 3013-3024, doi:10.1029/1998JB900090.

Irwin, G. R. (1957), Analysis of stresses and strains near the end of a crack traversing a plate, *J. Appl. Mech.*, *24*, 361–364.

Kostrov, B. V. (1964), Self similar problems of propagation of shear cracks, *J. Appl. Math. Mech.*, *28*, 889–898.

Lockner, D. A., and P. G. Okubo (1983), Measurements of frictional heating in granite, *J. Geophys. Res.*, *88*, 4313–4320.

Mai, P. M., and G. C. Beroza (2002), A spatial random field model to characterize complexity in earthquake slip, *J. Geophys. Res.*, *107*(B11), 2308, doi:10.1029/2001JB000588.

Mai, P. M., P. Sommerville, A. Pitarka, L. Dalguer, S. Song, G. Beroza, H. Miyake, and K. Irikura (2006), On scaling of fracture energy and stress drop in dynamic rupture models: Consequences for near-source ground-motions, in *Earthquakes: Radiated Energy and the Physics of Faulting*, *Geophys. Monogr. Ser.*, vol. 170, edited by R. Abercrombie et al., pp. 283–293, AGU, Washington, D. C.

McGarr, A., J. B. Fletcher, and N. M. Beeler (2004), Attempting to bridge the gap between laboratory and seismic estimates of fracture energy, *Geophys. Res. Lett.*, *31*, L14606, doi:10.1029/2004GL020091.

Ohnaka, M. (2003), A constitutive scaling law and a unified comprehension for frictional slip failure, shear fracture of intact rock, and earthquake rupture, *J. Geophys. Res.*, *108*(B2), 2080, doi:10.1029/2000JB000123.

Ohnaka, M., Y. Kuwahara, and K. Yamamoto (1987), Constitutive relations between dynamic physical parameters near a tip of the propagating slip zone during stick-slip shear failure, *Tectonophysics*, *144*, 109-125.

Okubo, P. G., and J. H. Dieterich (1986), State variable fault constitutive relations for dynamic slip, in *Earthquake Source Mechanics*, *Geophys. Monogr.*, vol. 37, edited by S. Das, J. Boatwright, and C. Scholz, pp. 25–35, AGU, Washington, D. C.

Otsuki, K. (2007), Dependence of surface fracture energy on earthquake size: A derivation from hierarchical self-similar fault zone geometry, *Geophys. Res. Lett.*, *34*, L20305, doi:10.1029/2007GL031419.

Palmer, A. C., and J. R. Rice (1973), The growth of slip surfaces in the progressive failure of overconsolidated clay, *Proc. R. Soc. London, Ser. A*, *332*, 527–548.

Paterson, M. S., and T.-F. Wong (2005), *Experimental Rock Deformation: The Brittle Field*, 2nd ed., 347 pp., Springer, New York.

Pittarello, L., G. Di Toro, A. Bizzarri, G. Pennacchioni, J. Hadizadeh, and M. Cocco (2008), Energy partitioning during seismic slip in pseudotachylyte-bearing faults (Gole Larghe Fault, Adamello, Italy), *Earth Planet. Sci. Lett.*, *269*, 131–139, doi:10.1016/j.epsl.2008.01.052.

Rice, J. R., C. G. Sammis, and R. Parsons (2005), Off-fault secondary failure induced by a dynamic slip pulse, *Bull. Seismol. Soc. Am.*, *95*, 109–134, doi:10.1785/0120030166.

Rudnicki, J. W. (1980), Fracture mechanics applied to Earth's crust, *Annu. Rev. Earth Planet. Sci.*, *8*, 489–525.

Ruina, A. L. (1983), Slip instability and state variable friction laws, *J. Geophys. Res.*, *88*, 10,359–10,370.

Schmedes, J., R. J. Archuleta, and D. Lavallée (2008), Spatial correlation between kinematic source parameters derived from dynamic rupture simulations, paper presented at the annual meeting, South. Calif. Earthquake Cent., Palm Springs, Calif.

Schmedes, J., R. J. Archuleta, and D. Lavallée (2010), Correlation of earthquake source parameters inferred from dynamic rupture simulations, *J. Geophys. Res.*, *115*, B03304, doi:10.1029/2009JB006689.

Sharon, E., S. P. Gross, and J. Fineberg (1996), Energy dissipation in dynamic fracture, *Phys. Rev. Lett.*, *76*, 2117–2120.

Song, S. G., A. Pitarka, and P. Sommerville (2009), Exploring spatial coherence between earthquake source parameters, *Bull. Seismol. Soc. Am.*, *99*, 2564–2571, doi:10.1785/0120080197.

Spudich, P., and M. Guatteri (2004), The effect of bandwidth limitations on the inference of earthquake slip-weakening distance from seismograms, *Bull. Seismol. Soc. Am.*, *94*, 2028–2036, doi:10.1785/0120030104.

Tada, H., P. C. Paris, and G. R. Irwin (2000), *The Stress Analysis of Cracks Handbook*, 3rd ed., 696 pp., Am. Soc. Mech. Eng., New York.

Tinti, E., P. Spudich, and M. Cocco (2005), Earthquake fracture energy inferred from kinematic rupture models on extended faults, *J. Geophys. Res.*, *110*, B12303, doi:10.1029/2005JB003644. (Correction, *J. Geophys. Res.*, *113*, B07301, doi:10.1029/2008JB005829, 2008.)

Venkataraman, A., and H. Kanamori (2004), Observational constraints on the fracture energy of subduction zone earthquakes, *J. Geophys. Res.*, *109*, B05302, doi:10.1029/2003JB002549.

Wilson, B., T. Dewers, Z. Reches, and J. Brune (2005), Particle size and energetics of gouge from earthquake rupture zones, *Nature*, *434*, 749–752, doi:10.1038/nature03433.

Wong, T. F. (1982), Shear fracture energy of Westerly granite from post-failure behavior, *J. Geophys. Res.*, *87*, 990–1000.

Yoshioka, N. (1996), Fracture energy and the variation of gouge and surface roughness during frictional sliding of rocks, *J. Phys. Earth*, *34*, 335–355.

Zhang, W., T. Iwata, K. Irikura, H. Sekiguchi, and M. Bouchon (2003), Heterogeneous distribution of the dynamic source parameters of the 1999 Chi-Chi, Taiwan, earthquake, *J. Geophys. Res.*, *108*(B5), 2232, doi:10.1029/2002JB001889.

A. Bizzarri, Istituto Nazionale di Geofisica e Vulcanologia, Sezione di Bologna, Via Donato Creti 12, I-40128 Bologna, Italy. (bizzarri@bo.ingv.it)